Fault parameters assessment from the gravity data profiles applying the global particle swarm optimization

Khalid Essa, Yves Géraud, Marc Diraison

▶ **To cite this version:**

Khalid Essa, Yves Géraud, Marc Diraison. Fault parameters assessment from the gravity data profiles applying the global particle swarm optimization. Journal of Petroleum Science and Engineering, 2021, 207, pp.109129. 10.1016/j.petrol.2021.109129 . hal-03698428

HAL Id: hal-03698428

https://hal.univ-lorraine.fr/hal-03698428

Submitted on 2 Aug 2023

HAL is a multi-disciplinary open access archive for the deposit and dissemination of scientific research documents, whether they are published or not. The documents may come from teaching and research institutions in France or abroad, or from public or private research centers.

L'archive ouverte pluridisciplinaire **HAL**, est destinée au dépôt et à la diffusion de documents scientifiques de niveau recherche, publiés ou non, émanant des établissements d'enseignement et de recherche français ou étrangers, des laboratoires publics ou privés.

Distributed under a Creative Commons Attribution - NonCommercial 4.0 International License

Version of Record: https://www.sciencedirect.com/science/article/pii/S0920410521007841
Manuscript_79f68eae624788cb0f1d7cd0a9584d03

Fault parameters assessment from the gravity data profiles applying the global particle swarm optimization

Khalid S. Essa[1*], Yves Géraud[2*], Marc Diraison[2*]

[1] Department of Geophysics, Faculty of Science, Cairo University, Giza, P.O. 12613, Egypt.

[2] Université de Lorraine, GeoRessources Laboratory, Nancy, 54500, France.

[*]Corresponding authors:

E-mail: khalid_sa_essa@yahoo.com

E-mail: yves.geraud@univ-lorraine.fr

E-mail: marc.diraison@univ-lorraine.fr

© 2021 published by Elsevier. This manuscript is made available under the CC BY NC user license
https://creativecommons.org/licenses/by-nc/4.0/

Abstract

This study focuses on interpreting gravity anomalies caused by fault structures. The faults types are the two-sided inclined fault, which represents mainly the normal and reverse faults, the two-sided vertical fault, the one-sided inclined fault, and the one-sided vertical fault. The study scheme is depends on the combination between the second moving average operator as a tool for separating the residual (desired) and regional (undesired) anomalies and then detecting the fault parameters applying the global particle swarm. The stability and efficiency of the proposed method has been applied to a synthetic example including the effect of regional background and to five real data sets from Iraq, USA, Egypt, and France. Available geologic and geophysical information supports our interpretation for the field examples from Iraq, USA, and Egypt. While, the forward model results from the detected parameters for the last field example (Pyrenees faults, France) was compared and matched well with measured gravity anomaly and found in a good agreement. So, this interpretation is open a sight-view for researchers around the world work in this area to use our results as a priori information for more investigations.

Keywords: Fault-like geologic structure; fault parameters; Bouguer anomaly; global particle swarm; hydrocarbon exploration.

1. Introduction

The gravity method is a non-invasive, cost-efficient and passive method, which measures the difference in the Earth's gravitational field at a certain location, caused by the rock mass properties (density). It has been applied in a wide range of projects such as hydrocarbon (oil and gas) exploration (Yuan et al., 2018; Saghafi and Yarveicy, 2019; Cho et al., 2020), underground cavities or tunnels detection (Pazzi et al., 2018; Abdullah et al., 2019; Saddek et al., 2019), geothermal exploration (Altwegg et al., 2015; Uwiduhaye et al., 2018), geotechnical and engineering application (Debeglia and Dupont, 2002; Arisona et al., 2018), weapons and unexploded ordnances inspections (Abedi et al., 2014), archaeology investigation (Branston and Styles, 2006; Batayneh et al., 2007; Sarlak and Aghajani, 2017), monitoring of ground water (Frappart and Ramillien, 2018; Delobbe et al., 2019), mineral and ores exploration (Hinze, 1960; Chen et al., 2015; Li et al., 2019; Essa and Abo-Ezz, 2021), landfills mapping (Silva et al., 2008; Gaël et al., 2017), radioactive waste management (An et al., 2013), mapping of subsurface structures (Chakravarthi et al., 2017; Deng et al., 2016; Essa et al., 2018).

The interpretation of gravity data was discussed in many studies and various approaches have been developed, which fall into the following categories:

1- The first category depends on using two-dimensional and three-dimensional forward modeling and inversion (Li and Oldenburg, 1998; Witter et al., 2016; Eshaghzadeh, 2018; Dai et al., 2019). The results from applying these methods assume that the subsurface information (density) is known a priori and require a large evaluation (time).

2- The second category include the application of structures with a simple geometry (spheres, cylinder, sheets and faults) which though they simplified geological elements,

give a good insight into the parameters of buried structures (depth, amplitude coefficient). Various graphical and numerical methods were developed for this case (Nettleton, 1976; Bowin et al., 1986; Shaw and Agarwal, 1990; Abdelrahman et al., 2006; Mehanee, 2014; Biswas, 2015; Mehanee and Essa, 2015; Tlas and Asfahani, 2018). However, these methods depend on human subjectivity, request a priori information about the form of buried objects, and depend upon certain point, which represent a strong limitation.

3- The third category is the application of global optimization algorithms to infer the geometry of buried structures from the gravity anomaly (Osman et al., 2006; Biswas, 2016; Roshan and Singh, 2017; Ekinci et al., 2019; Essa and Géraud, 2020; Mahmoodpour et al., 2020). These algorithms have been successively applied and delivered the optimum parameters.

2. Background study for estimating the fault parameters

Faults are discontinuities in the Earth's crust caused by stresses and are commonly subdivided based on their geometry and displacement into normal faults, reverse faults, strike-slip faults (Schultz, 2019; Brandes and Tanner, 2020). The displacement length is ranging from centimeters to several hundreds of kilometers and therefore important to recognize the nature, density and geometry distribution of these faults. So, the importance of studying and delineating the fault parameters, which include the amplitude coefficient, the depth to both or one-side, the dip angle, the location of the origin of the fault trace is very important in (1) recognizing the hydrocarbon system, (2) resolving many problem-related engineering applications, (3) delineating the associated mineralized or ore zones with faults, (4) helping in predicting the essential geological deformations events, (5)

93 monitoring the active shear zones in the subsurface, (6) delineating the hazards of
94 faulting before any investment planning, and (7) visualizing subsurface faults for more
95 scientific investigations.

96 Numerous scientists proposed various approaches for understanding gravity
97 anomaly due to this source. For example, Paul et al. (1966) indicated the usage of upward
98 continuation of the measured gravity anomaly for dip-angle estimation be dependent on
99 the Hilbert transform. Green (1976) mentioned the application of the vertical derivative
100 for gravity anomaly in dip angle estimation. However, these methods used a couple of
101 specific points and distances, and standardized curves which are considered a limitation.
102 Gupta and Pokhriyal (1990) proposed a method to evaluate a dip angle of two semi-
103 infinite thin horizontal layers displaced vertically (two-sided fault) applying the
104 maximum (g_{max}) and minimum (g_{min}) values on a gravity profile. However, they used a
105 few characteristic points to define the model parameters. Chakravarthi and Sundararajan
106 (2004) established an inversion approach using the iterative ridge-regression formula to
107 assess the parameters for fault structures, in addition to the influence of regional field
108 through an analytical formula for gravity anomalies of an inclined fault based on the
109 parabolic relationship between the depth and density contrast. However, the fault
110 structures frequently have finite strike lengths with the fault planes listric in nature.

111 Abdelrahman et al. (2013) applied a least-square method depends on evaluating
112 the window-curves between depth and the dip angle of the blind fault applying the first
113 moving average operator. The limitation behind applying the window-curves method was
114 trapped in a local minimum, i.e., intersected in several solutions and sometimes not
115 converges. Essa (2013) proposed a statistical method depending upon estimating the

variance for all assessed depths of the upthrown from first horizontal derivatives gravity anomalies through a least-squares sense assuming a range for the dip angle. However, the limitations for this method is categorized into the following: (1) the effect of noise have been noticed because of using a derivative-operator and (2) the precision of the results obtained depends on the accuracy to terminate the impact of the regional geological structure, which represents by a 1st-order polynomial only. Toushmalani (2013) suggested a heuristic global optimization method (PSO) to gravity data interpretation for the fault structure.

Abdelrahman and Essa (2015) established three successive least-squares minimization methods as follows: first least-squares minimization is to solve a nonlinear form in depth, then after estimated the depth, another nonlinear least-squares approach is used to evaluate the dip angle, lastly after the depth and dip angle estimation, a linear least-squares formula utilized to estimate the amplitude factor of a buried inclined fault applying the first moving average operator to confiscate a regional background up to 1st-order. This approach relies on describing the anomaly at the origin and zero- distance for each residual moving average gravity anomaly. Kusumot (2017) proposed an approach to estimate the dip angle of fault structures, which is dependent on applying the eigenvector of the observed or calculated gravity gradient tensor on a profile and exploring its properties through numerical simulations because the fault dip is a key parameter of a fault that has implications for hazard assessment. However, to get more accurate results about the dip angle, it needs more a priori geologic information. Essa et al. (2021) proposed a method to interpret a two-sided fault structure using the second horizontal derivative method to eliminate only a 1st-order regional background.

The research presented herein an extension of the global particle swarm optimization to interpret the residual gravity anomaly of a two-dimensional (2-D) fault structure. This method is dependent on using the second moving average operator to eradicate the regional background from the Bouguer gravity data and then applying this optimization to assess the fault parameters, which are the amplitude coefficient, the depth of the shallow-side (upthrown), the depth of the deep-side (downthrown), the dip angle, and the location of the fault trace.

Finally, the suggested approach was tested on a synthetic example that represents Bouguer gravity data across an inclined fault containing a 3rd-order regional field without and with 5% and 10% random noise to measure its robustness and consistency. The suggested method was also applied to five real field data sets collected across faults in Iraq, USA, Egypt, and France, in attempt to evaluate the robust and applicability of the link between the global particle swarm optimization and the second moving average method while applied to real gravity data.

3. The method

Observed gravity anomaly along a profile is given by the following form:

$$B_{ouguer}(x_j) = R_{esidual}(x_j, z) + R_{egional}(x_{j,}), \qquad j = 0, 1, 2, 3, \dots, N \qquad (1)$$

where $B_{ouguer}(x_j)$ represented the Bouguer or measured gravity data, $R_{esidual}(x_j, z)$ is the residual gravity anomaly for the two-dimensional fault structure that declared below, and $R_{egional}(x_j)$ represented the regional anomaly (Pawlowski, 1994; Obasi et al., 2016). The steps of this suggested methodology were mentioned as follow:

3.1 Forward modeling of the fault types

Gravity anomaly (g) formula (Telford et al., 1990; Hinze et al., 2013) for a dip-slip fault along the profile is:

$$g(x_j, z_1, z_2, \beta) = K\left\{1 + \frac{1}{\pi} tan^{-1}\left[\frac{(x_j - d)}{z_1} + \cot\beta\right] - \frac{1}{\pi} tan^{-1}\left[\frac{(x_j - d)}{z_2} + \cot\beta\right]\right\} \qquad (2)$$

where z_1 is the depth to the upper (shallow) side (km), z_2 is the depth to the lower (deep) side (km), $K = 2\pi f \Delta\sigma t$ is the amplitude coefficient (mGal) and it is a function in the density contrast and thickness of the fault and $\Delta\sigma$ is the density-contrast between the fault and its surroundings $\left({}^{g}/_{cc}\right)$, f is the gravitational constant, which is 6.67×10^{-11} $\left({}^{m^3}/_{kg \times s^2}\right)$, and t is the thickness (km), x_j is the measured points position (km), β is the inclination angle (deg.), d is place of the fault trace (km).

Figure 1 (a and b) represents the schematic diagram for the normal and reverse faults, in which the gravity anomaly along a profile is generated by applying Eq. (2) for these faults.

In case of $\beta = 90^o$, the term $\cot\beta = 0$ and represent a vertical fault, like a strike-slip fault (Figure 1c) and the gravity anomaly is:

$$g(x_j, z_1, z_2) = K\left\{1 + \frac{1}{\pi} tan^{-1}\left[\frac{(x_j - d)}{z_1}\right] - \frac{1}{\pi} tan^{-1}\left[\frac{(x_j - d)}{z_2}\right]\right\} \quad (3)$$

From Eq. (2), if the $\beta = 90^o$. So, the term $\cot\beta = 0$ and postulating that the depth of the lower part (deep) is equal infinity, i.e. $z_2 = \infty$. Hence, this two-sided inclined fault transformed into one-sided inclined shape (Figure 1d) and the gravity anomaly is:

$$g(x_j, z_1, \alpha) = K\left\{1 + \frac{1}{\pi} tan^{-1}\left[\frac{(x_j - d)}{z_1} + \cot\alpha\right]\right\} \quad (4)$$

For the similar two-sided vertical fault, in which $z_2 = \infty$, it is transformed into the one-sided vertical shape (Figure 1e) and the gravity anomaly is:

$$g(x_j, z_1) = K\left\{1 + \frac{1}{\pi} tan^{-1}\left[\frac{(x_j - d)}{z_1}\right]\right\} \quad (5)$$

3.2 Second moving average method

Numerous methods have been utilized for separating the Bouguer gravity anomaly into the effect of shallow structures (residual) and the effect of the deep structures (regional). The residual anomaly is calculated by subtracting the regional component from the Bouguer anomaly values. Thus, the second moving average operator is one of the prime methods in removing the gravity regional anomaly, which is signified by an empirical form up to a 3rd-order (Griffin, 1949; Essa and Munschy, 2019) is utilized. The second moving average regional anomaly along profiles is:

$$R_2(x_j, z, s) = \frac{6g(x_j) - 4g(x_j + s) - 4g(x_j - s) + g(x_j + 2s) + g(x_j - 2s)}{4}, \quad (6)$$

where s is the window lengths. Additionally, the gravity anomalies elucidation includes only a quite extended profile length, the short profiles lengths may considered as limitation in the interpretation. Therefore, overcoming this limitation efficiently and economically is done by increasing the collected measuring number points along a profile or digitizing the gravity profile applying an appropriate interval.

This method is easy and has a power to provide a high resolution in excluding the regional anomaly to the third-order polynomial effect from the Bouguer field through several filters of the consecutive window lengths. Besides, this method can be utilized for large gridded Bouguer data sets.

3.3 Global particle swarm

The global optimization particle swarm method is well-established and has been utilized to solve many geophysical problems (Shaw and Srivastava, 2007; Göktürkler and Balkaya, 2012; Singh and Biswas, 2016; Essa and Elhussein, 2018; Jamasb et al., 2019; Pace et al., 2019; Essa, 2020; Loni and Mehramuz, 2020; Moura et al., 2020). The particle swarm progression is stochastic and can be outlined by a population of particles known as a swarm. Each particle in the swarm has a location and speed vectors where the location vectors imply the assessment of the parameters.

This optimization is balanced with irregular models and searching for models by informing generations. In each iterative step, each model improves its speed and location using the following forms:

$$V_j^{k+1} = c_3 V_j^k + c_1 \mathrm{rand}\left(T_{best} - G_j^k\right) + c_2 \mathrm{rand}\left[\left(J_{best} - G_j^k\right)\right], \quad (7)$$

$$G_j^{k+1} = G_j^k + V_j^{k+1}. \quad (8)$$

where v_j^k is the j^{th} particle speed at the k^{th} iteration, G_j^k is the existent j^{th} particle location at the k^{th} iteration, rand is random numbers between $[0,1]$, c_1 and c_2 are equal 2 and so-called cognitive and social parameters (Parsopoulos and Vrahatis, 2002), c_3 is the inertial weight (= 0.8), which controls the speed of each particle. The motivation behind choosing and employing the swarm is to induce a global solution of numerous geometrical models from the gravity data rapidly and entails the noticeable the prominence of utilizing this algorithm among different conventional, non-conventional and optimization methods. Besides, a fast converging to the optimum-solution in real-time effects managing and well recital assessment. Moreover, we focus on its benefits in overcoming the ill-posed and non-unique nature of inversion of gravity data. Besides, it is stable, robust and efficient in reaching an optimum global solution. The theoretical and field models discussed-below illustrate the power of the method.

3.4 The inverse problem solutions

The inverse problem process is deciphered by assessing the set parameters that designate the buried fault structures from the gravity data. The inverse problem solution includes applying a preliminary model (Zhdanov, 2002; Mehanee et al., 2011). This start model could be generated by supposing a priori information from offered geologic, drilling, and other geophysical methods. The starter model is progressively adopted through the evaluation processes until getting the optimal model amongst the observed and detected data.

For the fault structure, the model parameters are the depth to the shallow side, the depth to the deep side, the amplitude coefficient, the dip angle, and the location of the

fault trace (the position of the fault). After estimating these parameters, the data fit (misfit) is assessed by using an objective function, which is minimized by a suitable algorithm. At the end of getting a robust model, it is considered as the most plausible geologic model.

Considering the buried geologic fault model is characterizing by a finite number of discrete parameters as follows:

$$\vec{P} = [P_1, P_2, P_3, \dots, P_m]^T, \qquad (9)$$

where, T indicates the matrix transpose.

Similarly, the Bouguer gravity data are collected into a vector (data vector), i.e. $\overrightarrow{g_p}$, as follows:

$$\overrightarrow{g_p} = \left[g_1^p, g_2^p, g_3^p, \dots, g_N^p\right]^T, \qquad (10)$$

In inverse modeling, it is presumed that there occurs a method to gauge such data from the components of the model vector to certain locations, which would be measured only when the structure is portrayed exactly by model and noiseless data. Let these synthetic data be arranged into the next N-dimensional vector:

$$\overrightarrow{g_c} = [g_1^c, g_2^c, g_3^c, \dots, g_N^c]^T, \qquad (11)$$

where g is an element of the Euclidean data space and c represents the evaluated data. For the essential postulation, there is a linking amongst vectors $\overrightarrow{g_p}$ and $\vec{p}$ as follows:

$$\overrightarrow{g_c} = \vec{g}(\vec{p}), \qquad (12)$$

where $\vec{g}$ represents a forward fault modeling. The whole error amongst the observed and modeled data sets is expressed by the deviation vector as follows:

$$\vec{E} = \overrightarrow{g_p} - \overrightarrow{g_c}. \qquad (13)$$

This equation is not null vector because the individual errors cannot be zero. Therefore, the search for an appropriate approach to solve and maintain the objective function, which is expressed by the following form:

$$\psi = \sqrt{\frac{1}{N}\sum_{i=1}^{N}[g_j^p - g_j^c]^2}\ , \qquad (14)$$

where N is the measured points, g_j^p is the Bouguer gravity anomaly and g_j^c is the estimated gravity anomaly at a certain point x_j. The best-fit solution of the parameters (K, z_1, z_2, β, and d) achieved by applying the above-mentioned objective function.

Finally, Figure 2 demonstrates the flow chart explaining the steps applied for the fault parameters evaluation of the suggested method. These steps are: (1) read the gravity data profile, (2) uses the second moving average method with numerous window lengths to eradicate the weight of the regional background, (3) applies the global particle swarm method to each residual anomaly to calculate the optimum-fit buried fault parameters, and (4) uses these parameters to determine the anticipated response, which is then matched vs. the observed gravity data.

3.5 Sensitivity analysis

Sensitivity analysis is a way to measures the impact of uncertainties of one or more input parameters of the model, which can led to uncertainty in the output model. Moreover, it can be used to explore the robust and the accuracy of the proposed method. Various methods have been used to predict the global model and reduced uncertainty in the final results such as Sobol (Sobol, 2001), Morris sensitivity analysis (King and Perera, 2013), distance-based generalized sensitivity analysis (Fenwick et al., 2014),

Bayesian Long Short-term Memory Networks (Feng, 2021). Also, Yin (2019) studied the application of Morris sensitivity analysis and Ensemble Smoother with Multiple Data Assimilation (ES-MDA) to investigate uncertainty parameters in reservoir models. The uncertainty and accuracy of the proposed method are studied through the application on synthetic model with different level of noise and five read data sets from different places, which are discussed below.

4. Application of the suggested method

The analysis and justification of the precision and the benefits of the proposed method for calculating the two-dimensional (2-D) fault model parameters were examined through a synthetic gravity anomaly, which demonstrated the effect of imposed a third-order regional background, and five real gravity data sets from Iraq, USA, Egypt, and France as follows:

4.1 Synthetic model

The suggested method was studied through a 100 km profile for synthetic inclined two-sided fault model of K = 100 mGal, z_1 = 4 km, z_2 = 9 km, β = 50°, d = 10 km and having a 3rd-order regional anomaly using the next formula:

$$\Delta g(x_j) = 100\left\{1 + \frac{1}{\pi} tan^{-1}\left[\frac{(x_j - 10)}{4} + \cot 50\right] - \frac{1}{\pi} tan^{-1}\left[\frac{(x_j - 10)}{9} + \cot 50\right]\right\} + 0.001x_j^3 + 0.002x_j^2 + 2x_j + 4\,. \quad (15)$$

The composite gravity anomaly (Δg) without and with various random noise level (5% and 10 %) is subjected to the suggested approaches as follows: First for the free-

316 noise data (Figure 3a), the second moving average operator was applied for several
317 window lengths (s-values) to eliminate the regional background (Figure 3b) and then
318 applied the global particle swarm for 100 models to assess the fault parameters (K, z_1, z_2,
319 β, and d), which are displayed in Table 1. Table 1 shows that the limits of each parameter
320 and the detected results for all parameters at several window lengths (s = 2, 3, 4, 5, 6, 7,
321 8, 9, and 10 km). Besides, it explains the average value (μ-value), uncertainty and the
322 percent of error (ϕ-value) in all parameters and the ψ-value that explains the misfit among
323 the Bouguer and assessed anomalies. In other words, Table 1 displays the limits of every
324 parameter; the amplitude coefficient (K) is between 50-300 mGal , depth of shallow side
325 (h_1) is between 1-20 km, depth of the deeper side (z_2) is between 1-20 km, the inclination
326 angle (β) is 10-180^o, and the location of the fault trace (origin; d) is between 1-20 km. So,
327 the μ-values for K, z_1, z_2, β, and d are 100 mGal, 4 km, 9 km, 50^o, and 10 km,
328 respectively. Besides, the ϕ-values and ψ-value for all parameter are equal zero.

329 The reliability of this method performance was investigated by introducing a 5%
330 random noise in the synthetic model declared-above (Figure 3c). In addition, Figure 3d
331 explains the second moving average residual gravity anomalies for s-value equals, 3, 4, 5,
332 6, 7, 8, 9, and 10 km. The predicated fault parameters by exploiting the particle swarm
333 for the assumed noisy model are offered in Table 1, which shows the μ-values for K, z_1,
334 z_2, β, and d as 97.2±1.1 mGal, 3.7±0.1 km, 8.6±0.1 km, 47.7±1.2^o, and 9.7±0.1, the ϕ-
335 values as 2.8%, 7.5%, 4.4%, 4.6%, and 3.0%, respectively, and the ψ-value is 9.7 mGal.
336 Also, the misfit was shown in Figure 3h.

337 Moreover, a 10% random was imposed the composite gravity anomaly (Δg)
338 (Figure 3e) to inspect the attainability of the present method. Using the similar

339 procedures, the second moving averages residual anomalies are exposed in Figure 3f and
340 the outcomes are presented and revealed in Table 1, which explains the estimated μ-
341 values for K, z_1, z_2, β, and d are 94.3±1.9 mGal, 3.5±0.2 km, 8.3±0.3 km, 44.9±2.0^o, and
342 9.4±0.2 km, the ϕ-values are 5.7%, 12.5%, 7.8%, 10.2%, and 6.0%, correspondingly. The
343 correlation between the Bouguer and the detected anomalies described, i.e., the ψ-value is
344 11.6 mGal. Furthermore, the geologic cross-section of the inclined two-sided fault was
345 represented in Figure 3g and the misfit between the Bouguer gravity anomaly and the
346 detected anomalies in each case was demonstrated in Figure 3h.
347 The attained fault parameters for noise-free and different noisy levels imposed in
348 the composite gravity anomaly explain that the proposed method has able to eliminate the
349 regional effect and noise and produced sound results.
350

351 ## 4.2 Field examples

352 To carefully inspect the applicability of the suggested method, five field examples
353 from Iraq, USA, France, and Egypt were investigated. The selected field examples were
354 examined to demonstrate the robustness and efficiency of applying the combined
355 between the second moving average operator and the global particle swarm algorithm.
356

357 ### 4.2.1 Field 1: Kifl oil field faults, Iraq

358 The Kifl area is located at the center of Iraq. This area contains a high thickness
359 (up to 8000 m) accumulation of sedimentary rocks and basement rocks. The age of these
360 sedimentary rocks and basement rocks is from Eocene in the SW to recent sediments in
361 the Euphrates area eastward. Besides, the Quaternary sediments characterized by faulting

were covering the entire area. These faults belong to the Euphrates zone and an associated with the Najd fault. This area is considered as the boundary between the stable and unstable shelf (Mesopotamia and Tigris unstable subzone). The Mesopotamia basin was established on the Arabian plate and bounded to the west of the Zagros thrust zone. Therefore, the study area is considered the boundary between the stable and unstable shelf and situated in the west flank of the Mesopotamia basin (Jassim and Goff, 2006; Mousa et al., 2017) (Fig. 4a).

Gravity anomaly along a line 4 profile (Al-Farhan et al. 2019; figure 12d) was applied to the current interpretation. The length of this profile is 16000 m and it is digitized at 250 m sampling intervals (Fig. 4b). This gravity profile was processed with the second moving average operator to terminate the regional anomaly impeded using numerous different window lengths (s = 500, 750, 1000, 1250, 1500, 1750, 2000, 2250, and 2500 m) (Fig. 4c). The particle swarm was utilized to estimate the fault parameters from these anomalies (Table 2). Table 2 shows that the evaluated results for the fault parameters at all s-values declared-above, the average value (μ-value), uncertainty, and the ψ-value, which demonstrates the misfit among the Bouguer and the detected anomalies. From Table 2, the results are K_{11} = -2.43±0.05 mGal, z_{11} = 1745.4±29.9 m, z_2 = 2342.4±28.1 m, β_{11} = 50.6±1.3^o, and d_{11} = 8926.3±31.8 m for F1, K_{12} = -2.61±0.08 mGal, z_{12} = 1641.6±14.4 m, z_2 = 2342.4±30.7 m, β_{12} = 43.3±3.5^o, and d_{12} = 14640.6±68.8 m for F2, and the ψ-value equals 0.07 mGal. The model produced from the estimated parameters is outlined in Figure 4b and a sketch diagram showing the buried fault was presented in Figure 4d. The misfit between the Bouguer gravity anomaly and the detected gravity anomaly was demonstrated in Figure 4e.

385 The geological model is shown in Figure 4d, which was created from the
386 estimated parameters of the two faults (F1 and F2) that form a graben structure, which is
387 a potential target for oil exploration. Finally, the model of the two faults using the
388 suggested method has good agreement with Al-Frahan et al. (2019) method results.
389

390 ### 4.2.2 Field 2: Garber oil field fault, USA

391 The Garber oil field is located in north-central Oklahoma, USA and was
392 discovered in 1916. The Garber oil field is located at the Nemaha Ridge, which extends
393 from the Oklahoma center into Kansas and Nebraska and is characterized by several
394 anticline structures (Carey, 1954). Besides the faults in this area, the rocks are classified
395 as Ordovician in age (oil produced) located below the Pennsylvanian unconformity (Gish
396 and Carr, 1929). This oil field plays an important role in supplying the main resources for
397 this state. Miser (1954) stated that strike-slip movements took place at this reverse fault
398 system during the Pennsylvanian (Fig. 5a).
399 A gravity anomaly profile with 20000 m length was taken from Ferris (1987) to estimate
400 the target fault structure parameters (Fig. 5b). The profile was digitized in intervals of
401 250 m and treated with the second moving average method to execute the regional
402 background field using various s-values (s = 500, 750, 1000, 1250, 1500, 1750, 2000,
403 2250, and 2500 m) (Fig. 5c). Moreover, these residual anomalies are interpreted through
404 the particle swarm to guess the fault parameters (K, z_1, z_2, β, and d) (Table 3). The results
405 in Table 8 are K = 1.58 mGal, z_1 = 720.1 m, β = 122.8^o, and d = 7985.2 m. It has to be
406 noticed that the estimated value for the deep side of the fault (z_2) is not presented,
407 because z_2 is located too deep (Fig. 5d). The comparison of the responses (Bouguer and

408 detected anomalies) are shown in Figure 5b and the misfit (ψ-value = 0.02 mGal)
409 between them is presented in Figure 5e.

410 The estimated results were compared with the drilling information and other
411 results estimated by using different approaches as damped least-squares (Murthy and
412 Krishnamacharyulu, 1990), singular value decomposition (Rao et al., 2003), and
413 differential evolution algorithm (Ekinci et al., 2019) (Table 4).

414

415 4.2.3 Field 3: Gazelle fault, Egypt

416 The Gazelle fault situated in the west of Lake Nasser, south of Aswan, Egypt.
417 This fault is trending N-S with a 35 km length. The area that contains the Gazelle fault is
418 characterized by upper Cretaceous sandstone and shale of the so-called Nubian
419 Formations with a flat-lying, and gently dip westward with thickness as ranging between
420 200 m and 400 m. The fault is a strike-slip fault with a normal-fault. A near-surface
421 damage zone with fractures is developed. This area is very important in evaluation
422 because its near to the Lake Nasser and High Dam. Moreover, it is characterized by
423 repeated earthquakes (Issawi, 1969; Woodward-Clyde Consultants, 1985; Sawires et al.,
424 2015) (Fig. 6a).

425 A Bouguer gravity profile measured along the Gazelle fault, west of Lake Nasser,
426 south of Aswan, Egypt was interpreted to assess the fault parameters using the suggested
427 method (Fig. 6b). The length of the gravity profile is about 5000 m and digitized in
428 intervals of 62.5 m. Following the same approach as described above for the full
429 complete interpretation of this anomaly, the second moving average residual gravity
430 anomalies were obtained for several s = 125, 187.5, 250, 312.5, 375, 437.5, 500, 562.5,

and 625 m) (Fig. 6c). Then, the global particle swarm was applied to estimate the parameters (Table 5). Table 5 explains the limits of all parameters as follows: K from 0.5 to 50 mGal, z_1 from 50 to 1500 m, z_2 from 50 to 1500 m, β from 5 to 180^o, and d from 500 to 5000 m. Also, Table 5 shows that the expected results for all parameters at each s-value, the average value (μ-value), uncertainty, and the ψ-value, which exhibits the misfit among the Bouguer and the gauged anomalies. Based on this approach, the expected results are K = 3.3±0.2 mGal, z_1 = 199.1±9.9 m, z_2 = 456.9±62.1 m, β = 54.4±1.6^o, and d = 2429.1±8.1 m, and the ψ-value is 1.1 mGal. The deduced forward model using the appraised parameters is explained in Figure 6b and a sketch diagram showing the buried fault was presented in Figure 6d. The misfit between the Bouguer gravity anomaly and the detected gravity anomaly is shown in Figure 6e.

Furthermore, this explanation agrees well with the results achieved from several published literatures (Table 6). Table 6 displays the comparison results for the estimated parameters (K, z_1, z_2, β, and d) with the results from drilling information (Evans et al., 1991; who demonstrated that the depth to the shallow-side is approximately 200 m) and published inversion methods such as a least-squares window curves method (Abdelrahman et al., 2013; they presented the depth to shallow side, z_1, equals 173 m and the inclination angle equals 62.5^o), the variance analysis method (Essa, 2013; who delineated the value of z_1 which equals 208 and β =40^o), three least-squares minimization approaches (Abdelrahman and Essa, 2015; they estimated the values of K, z_1, and β which are 2.4 mGal, 202 m, 57.7^{o,} respectively).

4.2.4 Field 4: Mersa Matruh fault, Egypt

The Marsa Matruh area is situated in the Northwestern coastal zone of Egypt and considered as a part of the north Western Desert, which has a great economic importance, because it contains some major hydrocarbon fields. The Mersa Matruh Basin has special importance, because of its position with respect to many nearby oil fields. Geologically, it is a part from the unstable shelf of Egypt. The exposed sedimentary rocks in this area are Middle Miocene (Marmarica Limestone Formation in all area) to Quaternary (includes Pleistocene represented by oolitic limestone, and Holocene deposits) in age. The northwestern coastal zone is characterized by folds and faults; most of them developed in the Late Cretaceous-Early Tertiary, and have a NE-SW direction that follows the trend of Syrian Arc system. The structures were caused predominantly by rotation of stresses between the Middle Cretaceous and the Tertiary and probably throughout the Quaternary (Fig. 7a) (Shata, 1955, Said, 1962; El Shazly and Shata, 1969; Holail, 1993).

The Mersa Matruh fault is a suitable example from the Mersa Matruh basin and trends NE-SW as evaluated from the boreholes stratigraphy MM (Mersa Matruh) and S (Siqueifa) in the study area (Fig. 7a). According to Said (1962) and Barakat and Darwish (1984), the fault is Lower Cretaceous in age, its throw is about 610 m, and the fault extends to more than 4000 m depth. Figure 7b shows a gravity profile of 43200 m length, which is digitized at an interval of 450 m. This Bouguer gravity profile was processed by the second moving average operator utilizing different s-value (s = 900, 1350, 1800, 2250, 2700, 3150, 3600, 4050, and 4500 m) (Fig. 7c). Next, the global particle swarm was used to the output moving average residual anomalies to achieve the fault parameters (Table 7). Table 7 presents the best fit detected results, which are K = 14.6±0.7 mGal, z_1

= 4014.5±130.9 m, z_2 = 4740.4±224.9 m, β = 88.1±1.8°, and d = 21755.2±58.8 m, and the ψ-value equals 0.2 mGal. The optimal model owing to the assessed parameters was drawn in Figure 7b and a sketch diagram displaying the buried fault was offered in Figure 7d. The misfit between the Bouguer gravity anomaly and the detected gravity anomaly is displaced in Figure 8e. The detected fault parameters are consistent with borehole information and with the results achieved from drilling and using other published resources (Table 8).

4.2.5 Field 5: Pyrenees faults, France

After a Mesozoic extensive, transtensive and/or transpressive history, the convergence of the Iberian and Eurasian plates since 85 Ma led to the edification of the Pyrenees (Teixell et al., 2018). The current orogen consists of a doubly vergent chain (figure XX). The Axial Zone (AZ) is mainly formed by exhumed Hercynian basement rocks. Northward, the North Pyrenean Fault (NPZ) limits the AZ and the North Pyrenean Zone (NPZ) made of Hercynian basement blocks and thick Mesozoic series. Southward, we find the fold-and-thrust belt of the South Pyrenean Zone (SPZ). The Aquitaine and Ebro flexural foreland basins are overthrust by the NPF and the SPZ, respectively (Fig. 8a) (Chevrot et al., 2018).

A gravity profile of length 72000 m was digitized at an interval of 1000 m (Fig. 8b). The Bouguer gravity profile was subjected to the same full interpretation workflow as described above. The second moving average residual gravity anomalies were obtained for several s = 2000, 3000, 4000, 5000, 6000, 7000, 8000, 9000, and 10000 m (Fig. 8c). Subsequently, the global particle swarm was applied to obtain the fault

parameters (Table 9). Table 9 and Figure 8d explain the best fit detected results for three faults (F_1, F_2, and F_3), which are detected during the interpretation. The optimum models produced from the estimated parameters were drawn in Figure 6d. The misfit (ψ-value equals 0.52 mGal) between the Bouguer gravity anomaly and the detected gravity anomaly is shown in Figure 8e.

Finally, the proposed method has been successively applied to interpret faults in hydrocarbon and mineral exploration projects in Iraq, USA, Egypt, and France and can be extended to explore different regions around the world.

5. Discussion

The estimated results of the synthetic model without random noise and even include different level of noise (5% and 10%) and included a regional background reflect the efficiency of the proposed method to extract the fault parameters (the amplitude coefficient, the depth to the upthrown block, the depth to the downthrown block, the dip angle and the position of the fault) and eliminate the impact of regional anomaly. Moreover, the results of the gravity data of different field data sets from Iraq, USA, France, and Egypt demonstrated the applicability of the proposed method.

In case of using gravity data Gravity anomaly along a line 4 profile in Kifl oil field, the depths of the two faults (F1 and F2) is compared with that obtained by Al-Frahan et al. (2019). Also, the results of the fault parameters (especially, the depth) in the Graber oil field area are reasonable and compared with other published results (Table 4). In addition, the results achieved due to gravity anomaly of the Gazelle area agrees very well with the results obtained from the drilling information (especially the depth of the

upthrown) and from other published method such as Abdelrahman et al. (2013), Essa (2013), and Abdelrahman and Essa (2015) (Table 6). Furthermore, the estimated model parameters, i.e. z_1 = 4014.5 m, in the case of Mersa Matruh area is compared with other obtained information from drilling (z_1 > 4000 m) and from published numerical methods such as Abdelrahman and Essa (2013) that the z_1 is equal 3940 m and Anderson et al. (2020) in which z_1 = 3982.5 m (Table 8). Finally, the interpretation of the gravity profile of Pyrenees area explains that the area included three faults (F_1, F_2, and F_3) that depth ranging from nearly 6000 m to 10850 m (Fig 8d). The delineating of these three faults will informative for more future investigations in this area. Moreover, the results for the real examples from Iraq, USA, and Egypt are found in good agreement with the drilling and published results.

Finally, the advantages of applying the present method are that it can be utilized for any search problem without a priori information with fast convergence, easy in use, computational efficient and stable in detecting the fault parameters compared with other published methods (Abdmouleh et al. 2017). However, this approach limitation is slow search around the global solution.

6. Conclusion

The proposed global optimization is accomplished to evaluate the parameters of the faults (the amplitude coefficient, the depth to the upthrown block, the depth to the downthrown block, the dip angle, and the position of the fault) from the gravity anomaly. This method firstly depends on appraising the second moving average residual anomalies using numerous window lengths to eliminate the regional background. Secondly, the global particle swarm is applied to evaluate the fault parameters. Synthetic data and field data hydrocarbon and mineral exploration projects in Iraq, USA, Egypt, and France are presented in our study that demonstrated the stability and efficiency of the proposed method. Therefore, the estimated parameters should be incorporated with the available geological and geophysical information to support solving any encountered up normal solutions in geophysical exploration. Due to these facts, the application of this method can be extended to solve numerous geophysical problems in the future.

Acknowledgments

Authors would like to thank Prof. Prof. Vural Sander Suicmez, Editor-in-Chief, Prof. Tahar AÏFA, Executive Editor, and all anonymous expert reviewers for their keen interest and valuable comments for improving the original manuscript. Also, I wish to thank GEODENERGIES for providing a financial support to finish this work under the Project DONUTS.

References

Abdelrahman, E.M., Abo-Ezz, E.R., Essa, K.S., El-Araby, T.M., Soliman, K.S., 2006. A least-squares variance analysis method for shape and depth estimation from gravity data. J. Geophys. Eng. 3, 143–153.

Abdelrahman, E.M., Essa, K.S., 2013. A new approach to semi-infinite thin slab depth determination from second moving average residual gravity anomalies. Explor. Geophys. 44, 185–191.

Abdelrahman, E.M., Essa, K.S., 2015. Three least-squares Minimization Approaches to Interpret Gravity Data Due to Dipping Faults. Pure Appl. Geophys. 172, 427–438.

Abdelrahman, E.M., Essa, K.S., Abo-Ezz, E.R., 2013. A least-squares window curves method to interpret gravity data due to dipping faults. J. Geophys. Eng. 10, 025003.

Abdullah, F.M.S., Al-Shuhail, A.A., Sanuade, O.A., 2019. Characterization of Subsurface Cavities using Gravity and Ground Penetrating Radar. J. Environ. Eng. Geophys. 24, 265–276.

Abedi, M., Mosazadeh, K., Dehghani, H., MadanchiZare, A. 2014. AN-EUL method for automatic interpretation of potential field data in unexploded ordnances (UXO) detection. JME 5, 67–77.

Abdmouleh, Z., Gastli, A., Ben-Brahim, L., Haouari, M., Al-Emadi, N.A., 2017. Review of optimization techniques applied for the integration of distributed generation from renewable energy sources. Rene. Energy 113, 266–280.

Al-Farhan, M., Oskooi, B., Ardestani, V.E., Abedi, M., Al-Khalidy, A., 2019. Magnetic and gravity signatures of the Kifl oil field in Iraq. J. Pet. Sci. Eng. 183, 106397.

592 Altwegg, P., Schill, E., Abdelfettah, Y., Radogna, P.V., Mauri, G., 2015. Toward fracture
593 porosity assessment by gravity forward modeling for geothermal exploration (Sankt
594 Gallen, Switzerland). Geothermics 57, 26–38.
595 An, Z., Di, Q., Wang, R.., Wang, M., 2013. Multi-geophysical Investigation of
596 Geological Structures in a Pre-selected High-level RadioactiveWaste Disposal Area
597 in Northwestern China. J. Environ. Eng. Geophys. 18, 137–146.
598 Anderson, N.L., Essa, K.S., Elhussein, M., 2020. A comparison study using Particle
599 Swarm Optimization inversion algorithm for gravity anomaly interpretation due to a
600 2D vertical fault structure. J. Appl. Geophy. 179, 104120.
601 Arisona, A., Nawawi, M., Khalil, A.E., Abdulrahman, A., 2018. Assessment of
602 Microgravity Anomalies of Soil Structure for Geotechnical 2D Models. J. Geosci.
603 Eng. Env. Tech. 03, 151–154.
604 Barakat, M.G., Darwish, M., 1984. Contribution to the lithostratigraphy of the Lower
605 Cretaceous sequence in Mersa Matruh area, North Western Desert, Egypt. Geol.
606 Soc. Egypt.
607 Batayneh, A., Khataibeh, J., Alrshdan, H., Tobasi, U., Al-Jahed, N., 2007. The use of
608 microgravity, magnetometry and resistivity surveys for the characterization and
609 preservation of an archaeological site at Ummer-Rasas, Jordan. Archaeol. Prospect.
610 14, 60–70.
611 Biswas, A., 2015. Interpretation of residual gravity anomaly caused by simple shaped
612 bodies using very fast simulated annealing global optimization. Geosci. Front. 6,
613 875–893.

614 Biswas, A., 2016. Interpretation of gravity and magnetic anomaly over thin sheet-type
615 structure using very fast simulated annealing global optimization technique. Model
616 Earth Syst. Environ. 2, 30.
617 Bowin C, Scheer E, Smith W., 1986. Depth estimates from ratios of gravity, geoid, and
618 gravity gradient anomalies. Geophysics, 51, 123–136.
619 Brandes, C., Tanner, D., 2020. Fault mechanics and earthquakes, in: Tanner, D., Brandes,
620 C. (Eds.), Understanding Faults: Detecting, Dating, and Modeling. Elsevier,
621 Amsterdam, pp. 11–80.
622 Branston, M.W., Styles, P., 2006. Site characterization and assessment using the
623 microgravity technique: a case history. Near Surf. Geophys. 4, 377–385.
624 Carey, L.W., 1954. The subsurface geology of the Garber area, Garfield County,
625 Oklahoma, in Shale Shaker Digest. Oklahoma City Geological Society 1, 384–
626 403.
627 Chakravarthi, V., Sundararajan, N., 2004. Ridge regression algorithm for gravity
628 inversion of fault structures with variable density. Geophysics 69, 1394–1404.
629 Chakravarthi, V., Mallesh, K., Ramamma, B., 2017. Basement depth estimation from
630 gravity anomalies: two 2.5D approaches coupled with the exponential density
631 contrast model. J. Geophys. Eng., 14, 303–315.
632 Chen, G.X., Liu, T.Y., Sun, J.S., Cheng, Q.M., Sahoo, B., Zhang, Z.J., Zhang, H.L.,
633 2015. Gravity method for investigating the geological structures associated with W-
634 Sn polymetallic deposits in the Nanling Range, China. J. Appl. Geophy. 120, 14–
635 25.

636 Chevrot, S., Sylvander, M., Diaz, J., Martin, R., Mouthereau, F., Manatschal, G., Masini,
637 E., Calassou, S., Grimaud, F., Pauchet, H., Ruiz, M., 2018. The non-cylindrical
638 crustal architecture of the Pyrenees. Sci. Rep. 8, 9591.
639 Cho, Y., Cao, Y., Zagayevskiy, Y., Wong, T., Munoz, Y., 2020. Kriging-based
640 monitoring of reservoir gas saturation distribution using time-lapse multicomponent
641 borehole gravity measurements: Case study, Hastings Field. J. Petrol. Sci. Eng. 190,
642 107054.
643 Dai, S., Zhao, D., Wang, S., Xiong, B., Zhang, Q., Li, K., Chen, L., Chen, Q., 2019.
644 Three-dimensional numerical modeling of gravity and magnetic anomaly in a
645 mixed space-wavenumber domain. Geophysics 84, 1JA–Z21.
646 Debeglia, N., Dupont, F., 2002. Some critical factors for engineering and environmental
647 microgravity investigations. J. Appl. Geophy. 50, 435–454.
648 Delobbe, L., Watlet, A., Wilfert, S., Van Camp, M., 2019. Exploring the use of
649 underground gravity monitoring to evaluate radar estimates of heavy rainfall
650 Laurent. Hydrol. Earth Syst. Sci. 23, 93–105.
651 Deng, Y., Chen, Y., Wang, P., Essa, K.S., Xub, T., Liang, X., Badal, J., 2016. Magmatic
652 underplating beneath the Emeishan large igneous province (South China) revealed
653 by the COMGRA-ELIP experiment. Tectonophysics 672-673, 16–23.
654 Ekinci YL, Balkaya Ç, Göktürkler G., 2019. Parameter estimations from gravity and
655 magnetic anomalies due to deep-seated faults: differential evolution versus
656 particle swarm optimization. Turk. J. Earth Sci. 28, 860–881.
657 El-Shazly, M., Shata, A., 1969. Geomorphology and pedology of Mersa Matruh area
658 (Western Mediterranean littoral zone). Desert Inst. Bull. l9, 1–28.

659 Eshaghzadeh, A., 2018. 2D and 3D Inverse Modeling of the Residual Gravity Field for a
660 Buried Deposit Mass. 2nd Conference on Geophysics for Mineral Exploration and
661 Mining, cp-566-00038.
662 Essa, K.S., 2013. Gravity interpretation of dipping faults using the variance analysis
663 method. J. Geophys. Eng. 10, 015003.
664 Essa, K.S., 2020. Self potential data interpretation utilizing the particle swarm method for
665 the finite 2D inclined dike: mineralized zones delineation. Acta Geod.
666 Geophys. 55, 203–221.
667 Essa, K.S., Elhussein, M., 2018. PSO (Particle Swarm Optimization) for Interpretation of
668 Magnetic Anomalies Caused by Simple Geometrical Structures. Pure Appl.
669 Geophys. 175, 3539–3553.
670 Essa, K.S., Abo-Ezz, E.R., 2021. Potential field data interpretation to detect the
671 parameters of buried geometries by applying a nonlinear least-squares
672 approach. Acta Geod. Geophys. https://doi.org/10.1007/s40328-021-00337-5.
673 Essa, K.S., Géraud, Y., 2020. Parameters estimation from the gravity anomaly caused by
674 the two-dimensional horizontal thin sheet applying the global particle swarm
675 algorithm. J. Petrol. Sci. Eng. 193, 107421.
676 Essa, K.S., Munschy, M., 2019. Gravity data interpretation using the particle swarm
677 optimization method with application to mineral exploration. J. Earth Syst. Sci. 128,
678 123.
679 Essa, K.S., Mehanee, S.A., Elhussein, M., 2021. Gravity data interpretation by a two-
680 sided fault-like geologic structure using the global particle swarm technique. Phys.
681 Earth Planet. Inter. 311, 106631.

682 Essa, K.S., Nady, A.G., Mostafa, M.S., Elhussein, M., 2018. Implementation of potential
683 field data to depict the structural lineaments of the Sinai Peninsula, Egypt. J.
684 Afr. Earth Sci. 147, 43–53.
685 Evans, K., Beavan, J., Simpson, D., 1991. Estimating aquifer parameters from analysis of
686 forced fluctuations in well level: An example from the Nubian Formation near
687 Aswan, Egypt: 1. Hydrogeological background and large-scale permeability
688 estimates. J. Geophys. Res. 96, B7, 12127–12137.
689 Feng, R., 2021. Uncertainty Analysis in Well Log Classification by Bayesian Long Short-
690 term Memory Networks. J. Petrol. Sci. Eng.
691 https://doi.org/10.1016/j.petrol.2021.108816
692 Fenwick, D., Scheidt, C., and Caers, J., 2014. Quantifying Asymmetric Parameter
693 Interactions in Sensitivity Analysis: Application to Reservoir Modeling. Math.
694 Geosci. 46, 493-511, 2014.
695 Ferris, C, 1987. Gravity anomaly resolution at the Garber field. Geophysics 52, 1570–
696 1579.
697 Fouad, S.F.A., 2010. Tectonic evolution of the Mesopotamia Foredeep in Iraq. Iraqi Bull.
698 Geo. Min. 6, 2.
699 Frappart, F., Ramillien, G., 2018. Monitoring Groundwater Storage Changes Using the
700 Gravity Recovery and Climate Experiment (GRACE) Satellite Mission: A Review.
701 Remote Sens. 10, 829.
702 Gaël, D., Tanguy, R., Nicolas, M., Frédéric, N., 2017. Assessment of multiple
703 geophysical techniques for the characterization of municipal waste deposit sites. J.
704 Appl. Geophy. 145, 74–83.

705 Gish, W.G. and R.M. Carr, 1929, Garber Field, Garfield County, Oklahoma in Structure
706 of Typical American Oil Fields. Am. Assoc. Petroleum Geol. Symposium 1, 176–
707 191.

708 Göktürkler, G., Balkaya, Ç., 2012. Inversion of self-potential anomalies caused by
709 simple-geometry bodies using global optimization algorithms, J. Geophys. Eng. 9,
710 498–507.

711 Green, R., 1976. Accurate determination of the dip angle of a geological contact using the
712 gravity method. Geophys. Prospect. 24, 265–272.

713 Griffin, W.R., 1949. Residual gravity in theory and practice. Geophysics 14, 39–58.

714 Gupta, O.P., Pokhriyal, S.K., 1990. New formula for determining the dip angle of a fault
715 from gravity data. SEG Program Expanded Abstracts 9, 646–649.

716

717 Hinze, W.J., 1960. Application of the Gravity Method to Iron Ore Exploration. Econ.
718 Geol. 55, 465–484.

719 Hinze, W.J., von Frese, R.R.B., Saad, A.H., 2013. Gravity and Magnetic Exploration:
720 Principles, Practices and Applications. Cambridge University Press, p.512.

721 Holail, H., 1993. Diagenetic trends of the Pleistocene calcareous ridges, Mersa Matruh
722 area, Egypt. Chemical Geology 106, 375–388

723 Issawi, B., 1969. The Geology of Kurkur-Dungul Area. Geological Survey of Egypt,
724 Paper 46, p. 102.

725 Jamasb, A., Motavalli-Anbaran, S.H., Ghasemi, K., 2019. A Novel Hybrid Algorithm of
726 Particle Swarm Optimization and Evolution Strategies for Geophysical Non-linear
727 Inverse Problems. Pure Appl. Geophys. 176, 1601–1613.

728 Jassim, S.Z., Goff, J.C., 2006. Geology of Iraq, Czech Republic. 80-7028-287-8pp. 341.

729 King, D.M., Perera, B.J.C., 2013. Morris method of sensitivity analysis applied to assess
730 the importance of input variables on urban water supply yield–A case study. J.
731 Hydrol. 477, 17–32.

732 Kusumot, S., 2017. Eigenvector of gravity gradient tensor for estimating fault dips
733 considering fault type. Prog. Earth Planet Sc. 4, 15.

734 Li ,Y., Oldenburg, D.W., 1998. 3-D inversion of gravity data. Geophysics 63, 109–119.

735 Li, Y., Melo, A., Martinez, C., Sun, J., 2019. Geology differentiation: A new frontier in
736 quantitative geophysical interpretation in mineral exploration. The Leading Edge
737 38, 60–66.

738 Loni, S., Mehramuz, M., 2020. Gravity field inversion using Improved Particle Swarm
739 Optimization (IPSO) for estimation of sedimentary basin basement depth. Contrib.
740 to Geophys. Geodesy 50, 303–323.

741 Mahmoodpour, S., Kamari, E., Esfahani, M.R., Mehr, A.K., 2020. Prediction of
742 cementation factor for low-permeability Iranian carbonate reservoirs using particle
743 swarm optimization-artificial neural network model and genetic programming
744 algorithm. J. Petrol. Sci. Eng., 108102.

745 Mehanee, S.A., 2014. Accurate and efficient regularized inversion approach for the
746 isolated gravity anomalies. Pure Appl. Geophys. 171, 1897–1937.

747 Mehanee, S.A., Essa, K.S., 2015. 2.5D regularized inversion for the interpretation of
748 residual gravity data by a dipping thin sheet: numerical examples and case studies
749 with an insight on sensitivity and non-uniqueness. Earth Planets Space 67, 130.

750 Mehanee, S., Essa, K.S., Smith, P., 2011. A rapid technique for estimating the depth and
751 width of a two-dimensional plate from self-potential data. J. Geophys. Eng. 8, 447–
752 456.
753 Miser, H.D., 1954. Geological Map of Oklahoma: Oklahoma Geological Survey.
754 Moura, F.A., Silva, S.A., de Araújo, J.M., Lucena, L.S., 2020. Progressive matching
755 optimisation method for FWI. J. Geophys. Eng. 17, 357–364.
756 Mousa, A., Mickus, K., Al-Rahim, A., 2017. The thickness of cover sequences in the
757 Western Desert of Iraq from a power spectrum analysis of gravity and magnetic
758 data. J. Asian Earth Sci. 138, 230–245.
759 Murthy, R.I.V., Krishnamacharyulu, S.K.G., 1990. Automatic inversion of gravity
760 anomalies of faults. Comput. Geosci. 16, 539–548.
761 Nettleton, L.L., 1976. Gravity and magnetic in oil prospecting. McGraw-Hill Book Co.,
762 p.463.
763 Obasi, A.I., Onwuemesi, A.G., Romanus, O.M., 2016. An enhanced trend surface
764 analysis equation for regional–residual separation of gravity data. J. Appl.
765 Geophys. 135, 90–99.
766 Osman, O., Albora, A.M., Ucan, O.N., 2006. A new approach for residual gravity
767 anomaly profile interpretations: Forced Neural Network (FNN). Ann. Geophys. 49,
768 1201–1208.
769 Pace, F., Santilano, A., Godio, A., 2019. Particle swarm optimization of 2D
770 magnetotelluric data. Geophysics 84, E125–E141.
771 Parsopoulos, K.E., Vrahatis, M.N., 2002. Recent approaches to global optimization
772 problems through particle swarm optimization. Nat. Comput. 1, 235–306.

773 Paul, M.K., Datta, S., Banerjee, B., 1966. Direct interpretation of two dimensional
774 structural fault from gravity data. Geophysics 31, 940–948.
775 Pawlowski, R.S., 1994. Green's equivalent-layer concept in gravity bandpass filter
776 design. Geophysics 59, 69–76.
777 Pazzi, V., Di Filippo, M., Di Nezza, M., Carlà, T., Bardi, F., Fontanelli, K., Intrieri, E.,
778 Fanti, R., 2018. Integrated geophysical survey in a sinkhole-prone area:
779 Microgravity, electrical resistivity tomographies, and seismic noise measurements
780 to delimit its extension. Eng. Geol. 243, 282-293.
781 Rao, M.M.M., Murty, R.T.V., Murthy, K.S.R., Vasudeva, R.Y., 2003. Application of
782 natural generalised inverse technique in reconstruction of gravity anomalies due to
783 a fault. Indian J. Pure Ap. Mat. 34, 31–47.
784 Roshan, R., Singh, U.K., 2017. Inversion of residual gravity anomalies using tuned PSO.
785 Geosci. Instrum. Method. Data Syst. 6, 71–79.
786 Saddek, B., Chemseddine, F., Djamel, B., Nabil, B., 2019. Surface and Subsurface
787 Investigations for the Detection and Mapping of Underground Karst Cav. J. Geol.
788 Soc. India 93, 228–234.
789 Saghafi, H., Yarveicy, H., 2019. Gas hydrate stability conditions: modeling on the basis
790 of gas gravity approach. Pet. Sci. Technol. 37, 1938–1945.
791 Said, R., 1962. The Geology of Egypt. Elsevier, Amsterdam, New York, p.377.
792 Sarlak, B., Aghajani, H., 2017. Archaeological investigations at Tepe Hissar-Damghan
793 using Gravity and Magnetics methods. J. Res. on Archaeometry 2, 19–34.
794 Sawires, R., Peláez, J., Fat-Helbary, R.E., Ibrahim, H.A., García-Hernández, M.T., 2015.
795 An updated seismic source model for Egypt. In: Moustafa A (ed). Earthquake

796 engineering-from engineering seismology to optimal seismic design of engineering
797 structures. InTech. ISBN: 978-953-51-4116-7.
798 Schultz, R., 2019. Introduction to Geologic Structural Discontinuities, in: Schultz, R.
799 (Eds), Geologic Fracture Mechanics. Cambridge University Press, Cambridge, pp.
800 1-26.
801 Shata, A., 1955. An introductory note to the geology of the northern portion of the
802 western desert of Egypt. Bull. Desert Inst., Cairo 5, 96-106.
803 Shaw, R., Srivastava, S., 2007. Particle Swarm Optimization. A new tool to invert
804 geophysical data. Geophysics 72, F75–F83.
805 Shaw, R.K., Agarwal, P., 1990. The application of Walsh transforms to interpret gravity
806 anomalies due to some simple geometrical shaped causative sources: A feasibility
807 study. Geophysics, 55, 843–850.
808 Silva, J., Teixeira, W., Barbosa, V., 2008. Gravity data as a tool for landfill study.
809 Environ. Geol. 57:749–757.
810 Singh, A., Biswas, A., 2016. Application of global particle swarm optimization for
811 inversion of residual gravity anomalies over geological bodies with idealized
812 geometries. Nat. Resour. Res. 25, 297–314.
813 Sobol, I.M., 2001. Global sensitivity indices for nonlinear mathematical models and their
814 Monte Carlo estimates. Math. Comput. Simul. 55, 271–280.
815 Teixell, A., Labaume, P., Ayarza, P., Espurt, N., de Saint Blanquat, M., Lagabrielle, Y.,
816 2018. Crustal structure and evolution of the Pyrenean-Cantabrian belt: A review
817 and new interpretations from recent concepts and data. Tectonophysics 724–725,
818 146–170.

819 Telford, W.M., Geldart, L.P., Sheriff, R.E., 1990. Applied geophysics (2nd edition).
820 Cambridge University Press, p.770.
821 Tlas, M., Asfahani, J., 2018. Interpretation of gravity anomalies due to simple geometric-
822 shaped structures based on quadratic curve regression. Contrib. to
823 Geophys. Geodesy. 48, 161–178.
824 Toushmalani, R., 2013. Gravity inversion of a fault by Particle swarm optimization
825 (PSO). SpringerPlus 2, 315.
826 Uwiduhaye, J., Mizunaga, H., Saibi, H., 2018. Geophysical investigation using gravity
827 data in Kinigi geothermal field, northwest Rwanda. J. Afr. Earth Sci. 139, 184–192.
828 Witter, J.B., Siler, D.L., Faulds, J.E., Hinz, N.H., 2016. 3D geophysical inversion
829 modeling of gravity data to test the 3D geologic model of the Bradys geothermal
830 area, Nevada, USA. Geotherm. Energy 4, 14.
831 Woodward-Clyde Consultants (WCC), 1985. Identification of earthquake sources and
832 estimation of magnitudes and recurrence intervals. Internal Report High and Aswan
833 Dams Authority, Egypt, p.135.
834 Yin, Z., Feng, T., MacBeth, C., 2019. Fast assimilation of frequently acquired 4D seismic
835 data for reservoir history matching. Comput. Geosci. 128, 30–40.
836 Yuan, B., Song, L., Han, l., An, S., Zhang, C., 2018. Gravity and magnetic field
837 characteristics and hydrocarbon prospects of the Tobago Basin. Geophys. Prospect.
838 66, 1586–1601.
839 Zhdanov, M.S., 2002. Geophysical inversion theory and regularization problems,
840 Elsevier, Amsterdam, p.633.
841

Figure captions

Figure 1. Fault types analyzed in this study. A) Dip-slip fault with normal fault kinematics. Fault dips to the left. B) Dip-slip fault with reverse fault kinemantics. Fault dips to the right. C) Strike-slip fault with normal or reverse component. D) Dip-slip fault with limited data on the hanging wall block.

Figure 2. Flow chart for the proposed method.

Figure 3. (a) Noise-free composite anomaly (K = 100 mGal, z_1 = 4 km, z_2 = 9 km, β = 50^o, d = 10 km, and profile length = 100 km) and a deep seated regional structure. (b) Second moving average residual gravity anomalies for the anomaly in Figure 3a. (c) A 5% noise imposed in gravity anomaly of Figure 3a. The detected anomaly (blue dots) is also shown. (d) Second moving average residual gravity anomalies for the anomaly in Figure 3c. (e) A 10% noise imposed in the anomaly in Figure 3a. The detected anomaly (orange dots) is also shown. (f) Second moving average residual gravity anomalies for the anomaly shown in Figure 3e. (g) Sketch diagram of a buried fault model. (h) Misfit among the observed and detected anomalies in all cases.

Figure 4. (a) Location and geologic map of the Kifl oil field area, Iraq (after Al-Farhan et al., 2019). (b) Observed and detected gravity anomalies for the Kifl oil field, Iraq. (c) Second moving average residual gravity anomalies for the anomaly in Figure 4a. (d) Geologic sketch of a buried fault model. (e) Misfit among the observed and detected anomalies.

Figure 5. (a) Geologic map of the Garber oil field area, USA (after Ferris, 1987). (b) Observed and detected gravity anomalies for the Garber oil field, USA. (c)

865 Second moving average residual gravity anomalies for the anomaly in Figure
866 5a. (d) Sketch diagram of a buried model. (e) Misfit among the observed and
867 detected anomalies.
868 Figure 6. (a) Location and geologic map of the Gazelle fault, west of Lake Nasser, south
869 of Aswan, Egypt (after WCC, 1985). (b) Observed and detected gravity
870 anomalies for the Gazelle fault, Egypt. (c) Second moving average residual
871 gravity anomalies for the anomaly in Figure 6a. (d) Sketch diagram of a buried
872 model. (e) Misfit among the observed and detected anomalies.
873 Figure 7. (a) Location and ggeologic map of the Mersa Matruh basin, Egypt (after Holail,
874 1993). (b) Observed and detected gravity anomalies for the Mersa Matruh
875 fault, Egypt. (c) Second moving average residual gravity anomalies of the
876 observed anomaly in Figure 7a. (d) Geologic sketch of a buried model. (e)
877 Misfit among the observed and detected anomalies.
878 Figure 8. (a) Location and geologic map of the Pyrenees area, France (after Chevrot et
879 al., 2018). (b) The observed and detected gravity anomalies for the Pyrenees
880 area, France. (c) Second moving average residual gravity anomalies for the
881 anomaly in Figure 8a. (d) Sketch diagram for the buried multi-fault models. (e)
882 Misfit among the observed and detected anomalies.

(a)

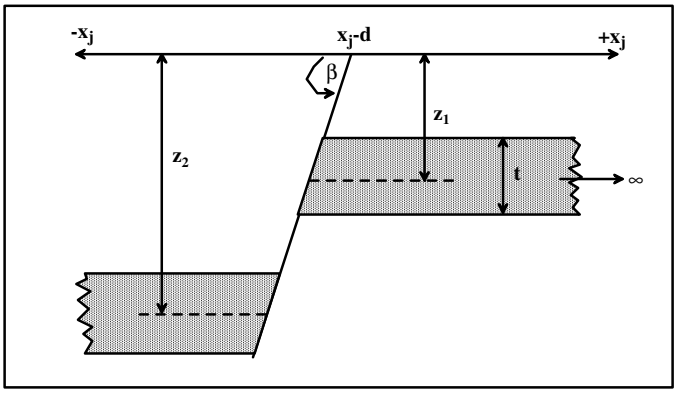
-xj
xj-d
+xj
β
z1
z2
t
∞

(b)

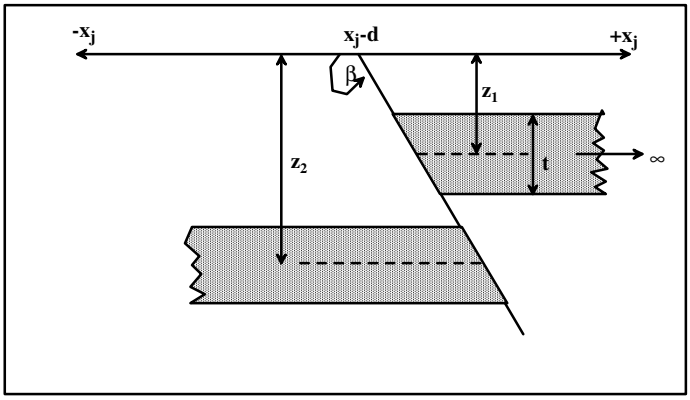
-xj
xj-d
+xj
β
z1
z2
t
∞

(c)

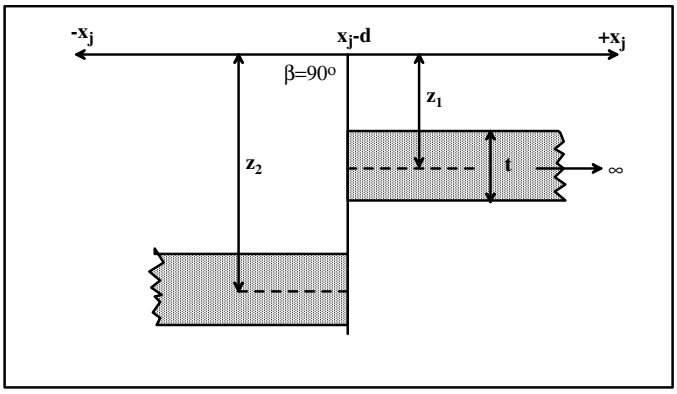
-xj
xj-d
+xj
β=90o
z1
z2
t
∞

(d)

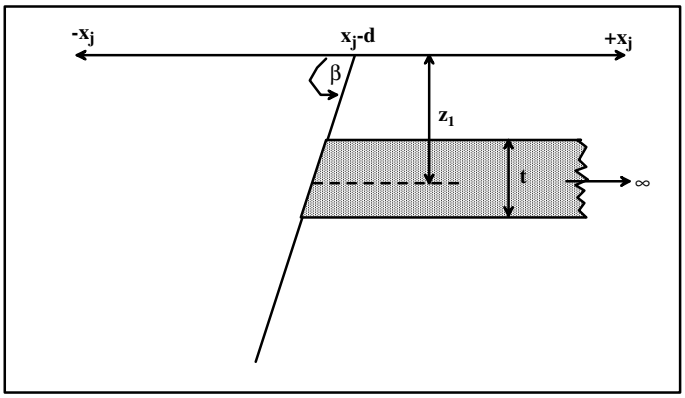
-xj
xj-d
+xj
β
z1
t
∞

(e)

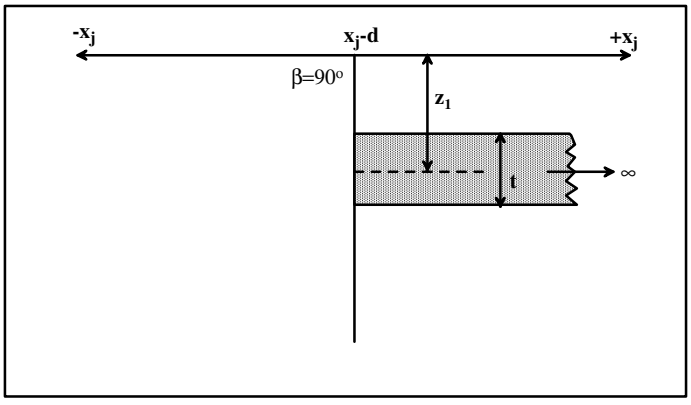
-xj
xj-d
+xj
β=90o
z1
t
∞

Fig. 1.

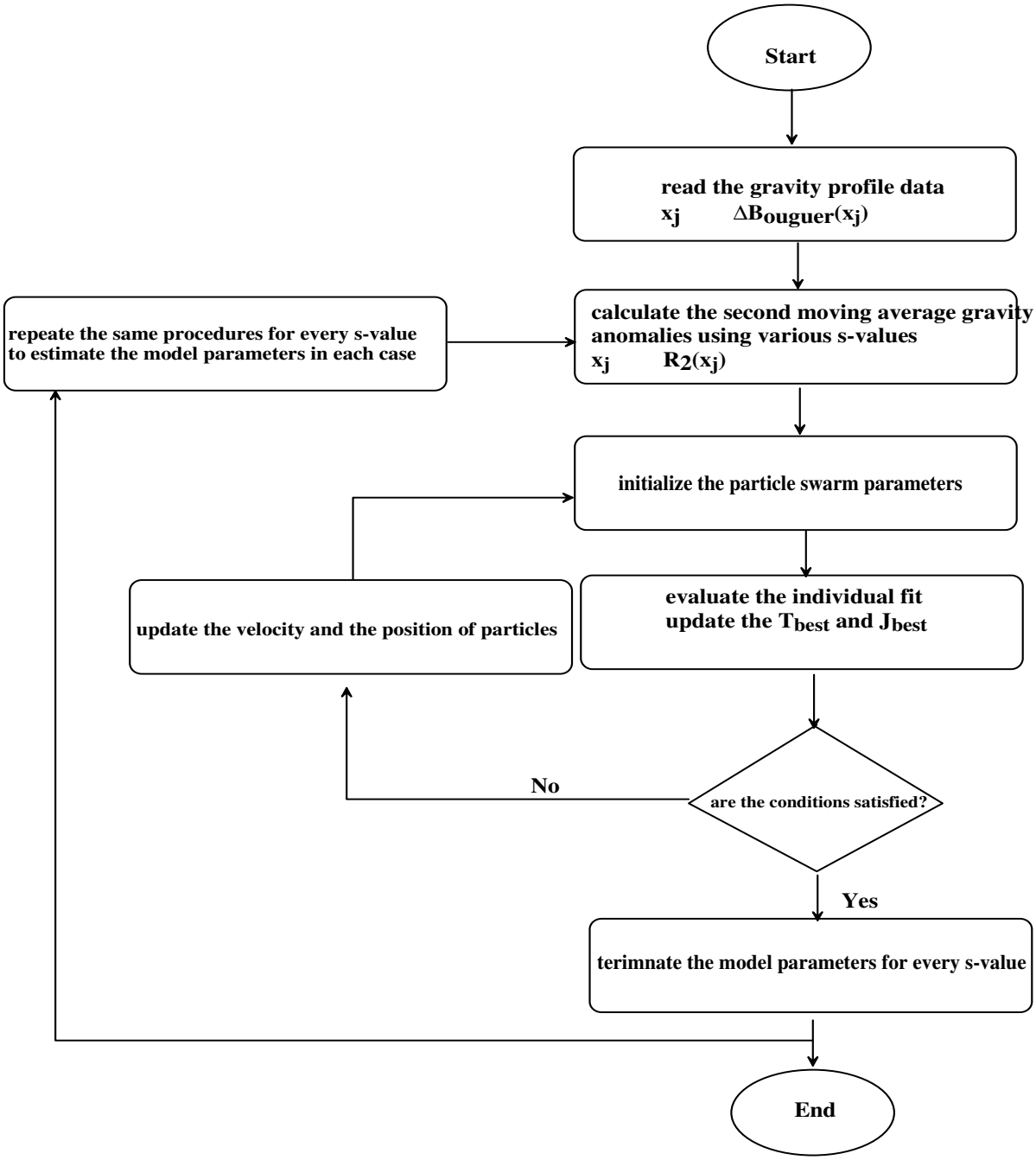
Start
read the gravity profile data
x_j $\Delta B_{ouguer}(x_j)$
calculate the second moving average gravity anomalies using various s-values
x_j $R_2(x_j)$
repeate the same procedures for every s-value to estimate the model parameters in each case
initialize the particle swarm parameters
evaluate the individual fit
update the T_{best} and J_{best}
update the velocity and the position of particles
are the conditions satisfied?
No
Yes
terimnate the model parameters for every s-value
End

Fig. 2.

(a)

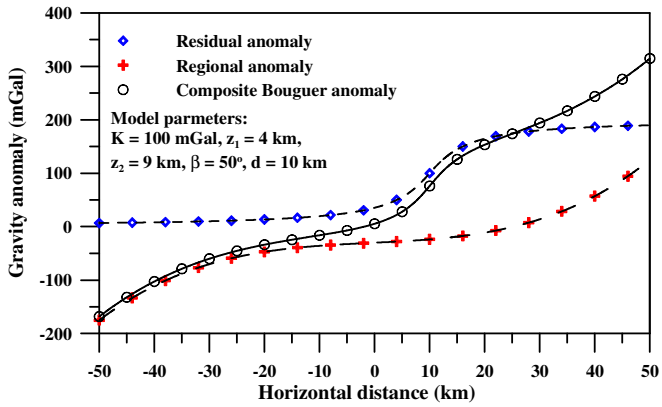
Residual anomaly
Regional anomaly
Composite Bouguer anomaly
Model parmeters:
K = 100 mGal, z1 = 4 km,
z2 = 9 km, β = 50°, d = 10 km
Gravity anomaly (mGal)
Horizontal distance (km)

(b)

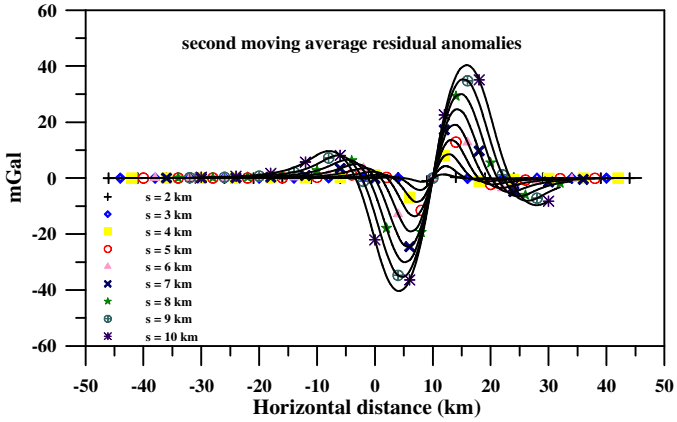
second moving average residual anomalies
mGal
s = 2 km
s = 3 km
s = 4 km
s = 5 km
s = 6 km
s = 7 km
s = 8 km
s = 9 km
s = 10 km
Horizontal distance (km)

(c)

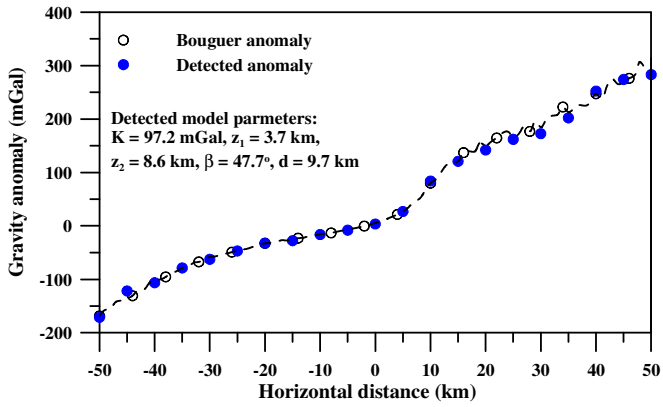
Bouguer anomaly
Detected anomaly
Detected model parmeters:
K = 97.2 mGal, z1 = 3.7 km,
z2 = 8.6 km, β = 47.7°, d = 9.7 km
Gravity anomaly (mGal)
Horizontal distance (km)

(d)

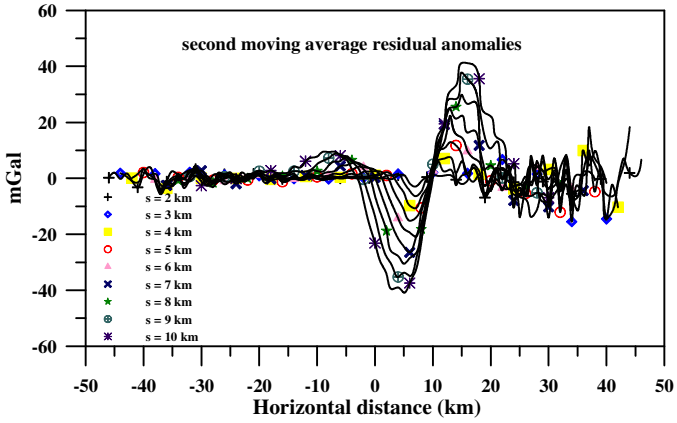
second moving average residual anomalies
mGal
s = 2 km
s = 3 km
s = 4 km
s = 5 km
s = 6 km
s = 7 km
s = 8 km
s = 9 km
s = 10 km
Horizontal distance (km)

(e)

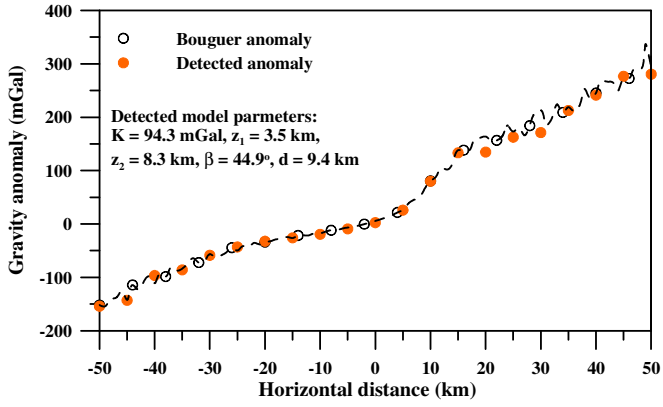
Bouguer anomaly
Detected anomaly
Detected model parmeters:
K = 94.3 mGal, z1 = 3.5 km,
z2 = 8.3 km, β = 44.9°, d = 9.4 km
Gravity anomaly (mGal)
Horizontal distance (km)

(f)

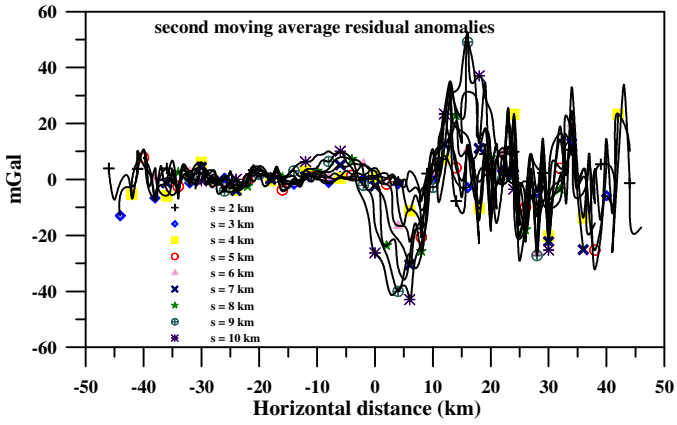
second moving average residual anomalies
mGal
s = 2 km
s = 3 km
s = 4 km
s = 5 km
s = 6 km
s = 7 km
s = 8 km
s = 9 km
s = 10 km
Horizontal distance (km)

(g)

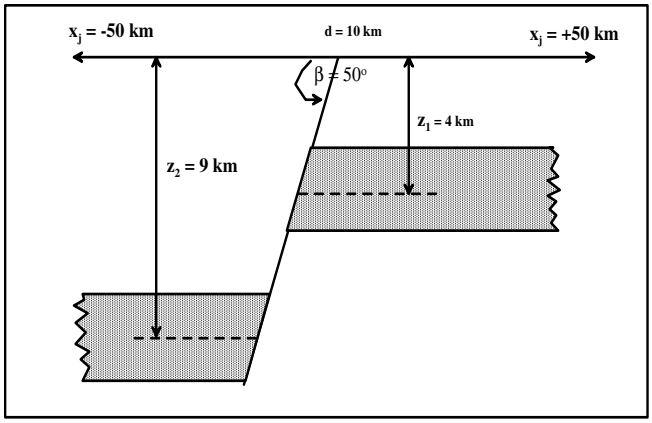
x_j = -50 km
d = 10 km
x_j = +50 km
β = 50°
z_1 = 4 km
z_2 = 9 km

(h)

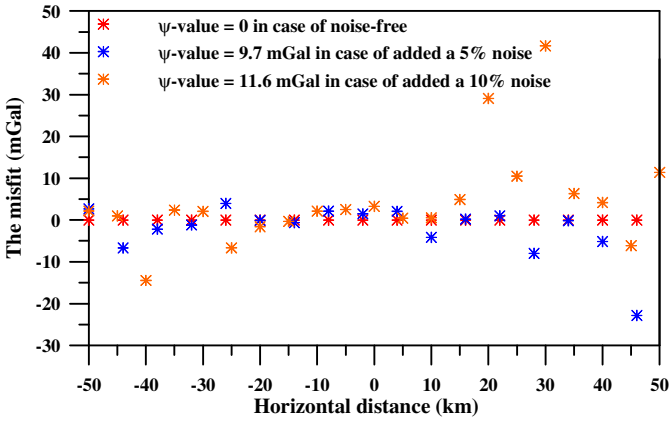
ψ-value = 0 in case of noise-free
ψ-value = 9.7 mGal in case of added a 5% noise
ψ-value = 11.6 mGal in case of added a 10% noise
The misfit (mGal)
Horizontal distance (km)
50
40
30
20
10
0
-10
-20
-30
-50
-40
-30
-20
-10
0
10
20
30
40
50

Fig. 3.

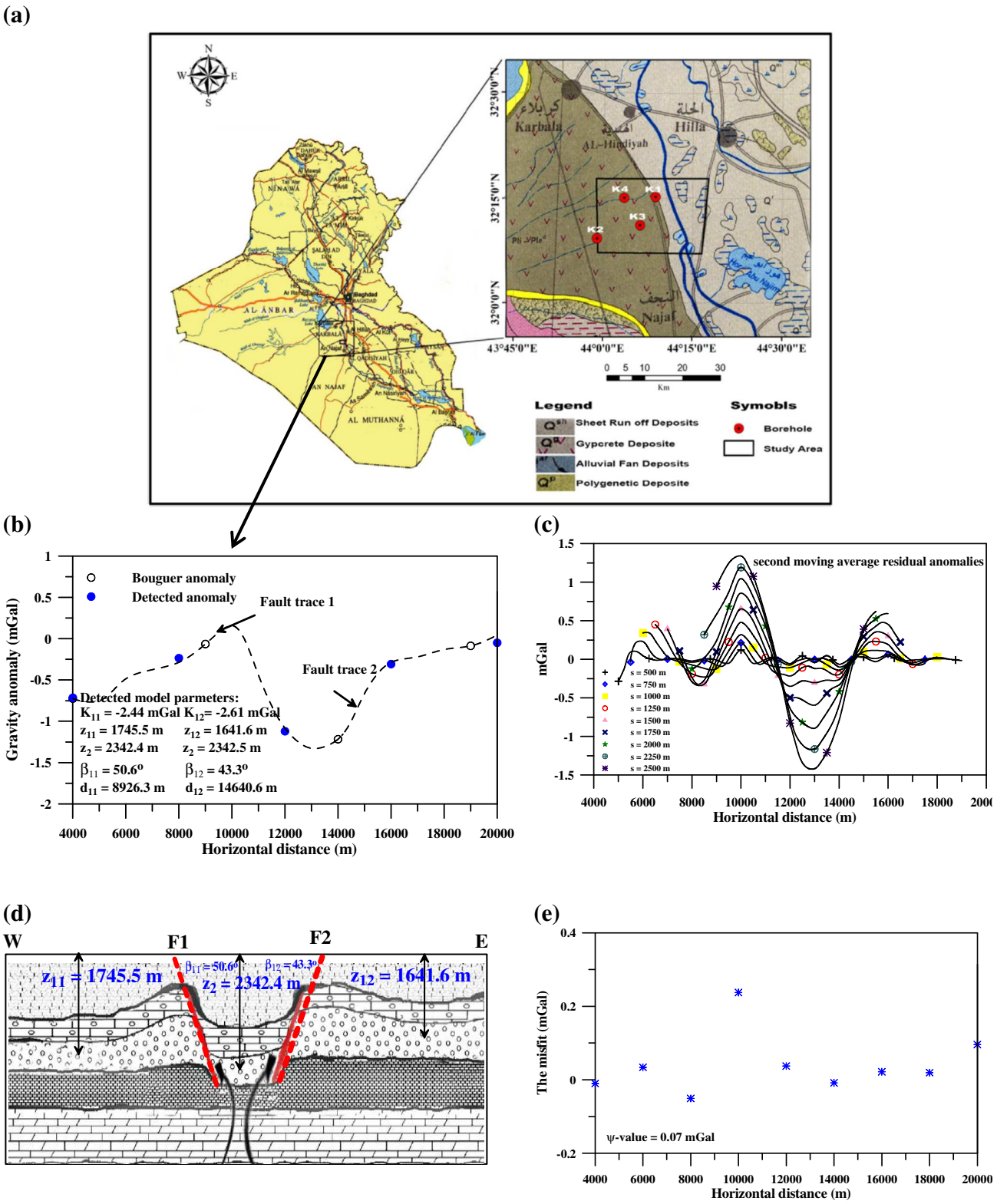
(a)
Karbala
Hilla
Najaf
Legend
Sheet Run off Deposits
Gyporete Deposite
Alluvial Fan Deposits
Polygenetic Deposite
Symobls
Borehole
Study Area
(b)
Bouguer anomaly
Detected anomaly
Fault trace 1
Fault trace 2
Detected model parmeters:
K11 = -2.44 mGal K12= -2.61 mGal
z11 = 1745.5 m z12 = 1641.6 m
z2 = 2342.4 m z2 = 2342.5 m
β11 = 50.6° β12 = 43.3°
d11 = 8926.3 m d12 = 14640.6 m
Gravity anomaly (mGal)
Horizontal distance (m)
(c)
second moving average residual anomalies
mGal
Horizontal distance (m)
(d)
W
F1
F2
E
z11 = 1745.5 m
z2 = 2342.4 m
z12 = 1641.6 m
(e)
The misfit (mGal)
ψ-value = 0.07 mGal
Horizontal distance (m)

Fig. 4.

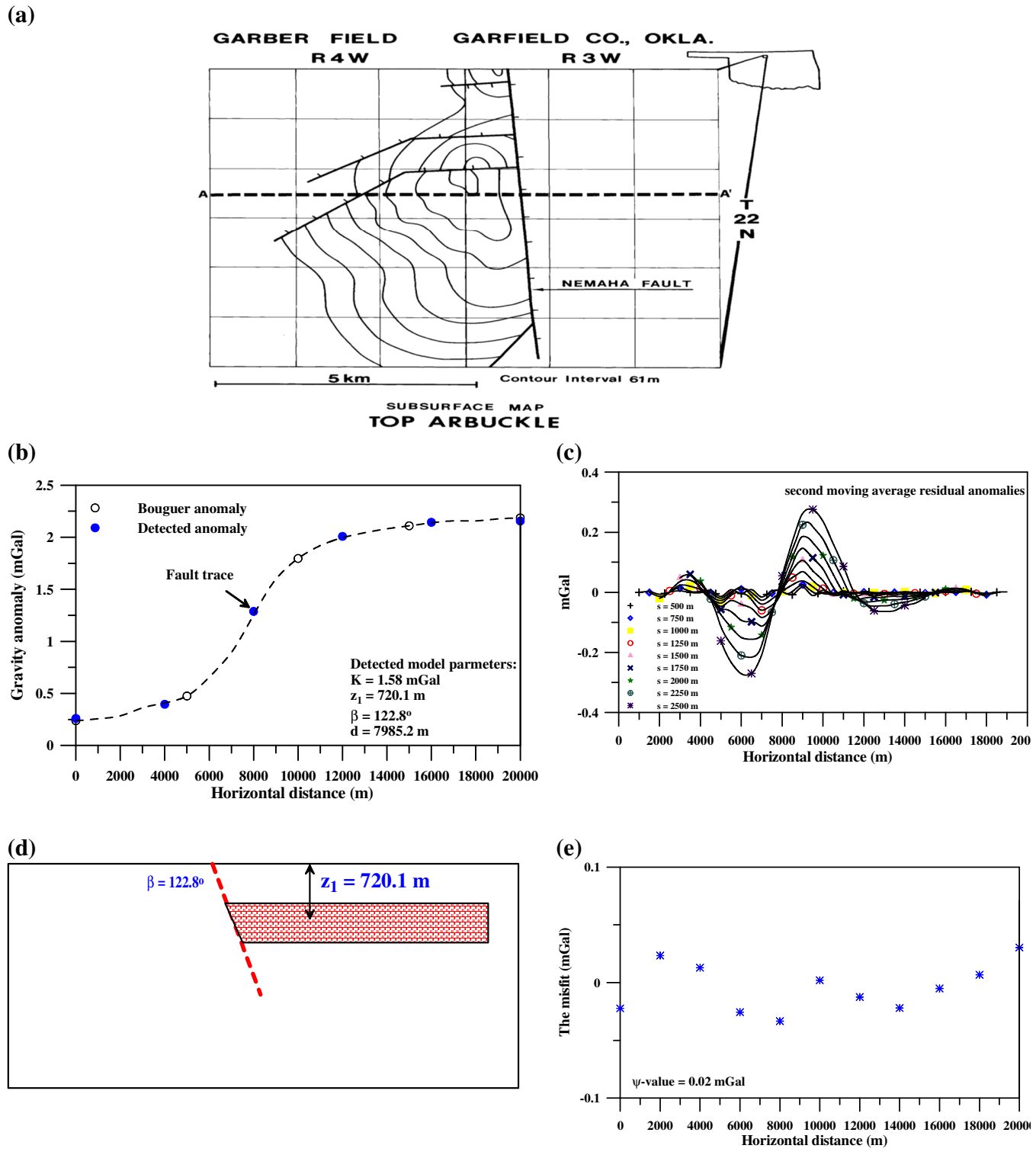
(a)
GARBER FIELD
R 4 W
GARFIELD CO., OKLA.
R 3 W
A
A'
T
22
N
NEMAHA FAULT
5 km
Contour Interval 61m
SUBSURFACE MAP
TOP ARBUCKLE
(b)
Bouguer anomaly
Detected anomaly
Fault trace
Detected model parmeters:
K = 1.58 mGal
z1 = 720.1 m
β = 122.8°
d = 7985.2 m
Gravity anomaly (mGal)
Horizontal distance (m)
(c)
second moving average residual anomalies
mGal
s = 500 m
s = 750 m
s = 1000 m
s = 1250 m
s = 1500 m
s = 1750 m
s = 2000 m
s = 2250 m
s = 2500 m
Horizontal distance (m)
(d)
β = 122.8°
z1 = 720.1 m
(e)
The misfit (mGal)
ψ-value = 0.02 mGal
Horizontal distance (m)

Fig. 5.

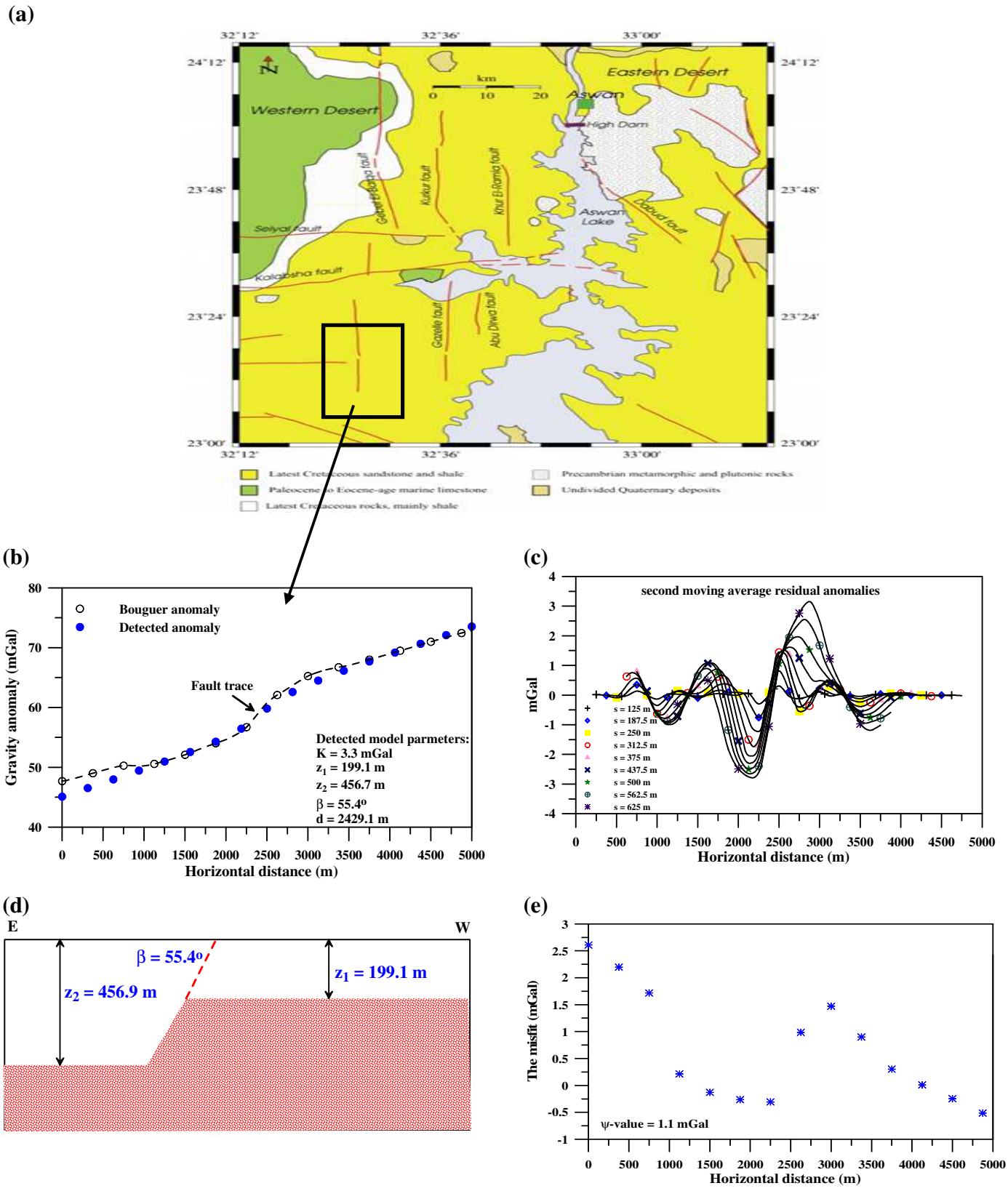
(a)
32°12'
32°36'
33°00'
24°12'
23°48'
23°24'
23°00'
N
km
0
10
20
Western Desert
Eastern Desert
Aswan
High Dam
Aswan Lake
Selyal fault
Kalabsha fault
Gebel Rokab fault
Kukur fault
Khur El Romia fault
Dakud fault
Gazelle fault
Abu Diwa fault
Latest Cretaceous sandstone and shale
Paleocene to Eocene-age marine limestone
Latest Cretaceous rocks, mainly shale
Precambrian metamorphic and plutonic rocks
Undivided Quaternary deposits
(b)
Bouguer anomaly
Detected anomaly
Fault trace
Detected model parmeters:
K = 3.3 mGal
z1 = 199.1 m
z2 = 456.7 m
β = 55.4°
d = 2429.1 m
Gravity anomaly (mGal)
Horizontal distance (m)
(c)
second moving average residual anomalies
mGal
s = 125 m
s = 187.5 m
s = 250 m
s = 312.5 m
s = 375 m
s = 437.5 m
s = 500 m
s = 562.5 m
s = 625 m
Horizontal distance (m)
(d)
E
W
β = 55.4°
z2 = 456.9 m
z1 = 199.1 m
(e)
The misfit (mGal)
ψ-value = 1.1 mGal
Horizontal distance (m)

Fig. 6.

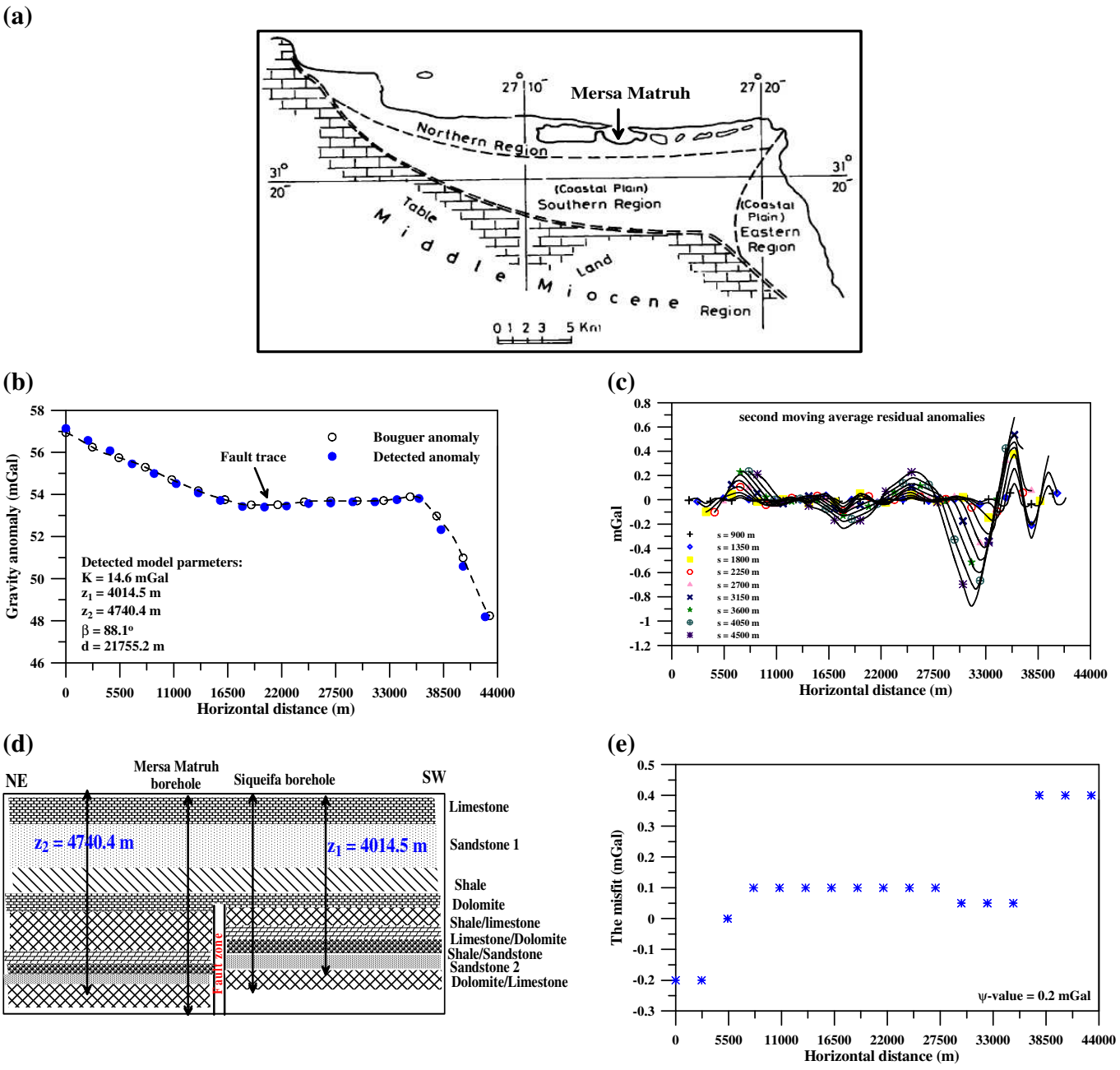
(a)
Mersa Matruh
27° 10′
27° 20′
31° 20′
Northern Region
(Coastal Plain)
Southern Region
(Coastal Plain)
Eastern Region
Table
Middle
Land
Miocene
Region
0 1 2 3 5 Km
(b)
Gravity anomaly (mGal)
Bouguer anomaly
Detected anomaly
Fault trace
Detected model parmeters:
K = 14.6 mGal
z1 = 4014.5 m
z2 = 4740.4 m
β = 88.1°
d = 21755.2 m
Horizontal distance (m)
(c)
second moving average residual anomalies
mGal
s = 900 m
s = 1350 m
s = 1800 m
s = 2250 m
s = 2700 m
s = 3150 m
s = 3600 m
s = 4050 m
s = 4500 m
Horizontal distance (m)
(d)
NE
Mersa Matruh borehole
Siqueifa borehole
SW
z2 = 4740.4 m
z1 = 4014.5 m
Fault zone
Limestone
Sandstone 1
Shale
Dolomite
Shale/limestone
Limestone/Dolomite
Shale/Sandstone
Sandstone 2
Dolomite/Limestone
(e)
The misfit (mGal)
ψ-value = 0.2 mGal
Horizontal distance (m)

Fig. 7.

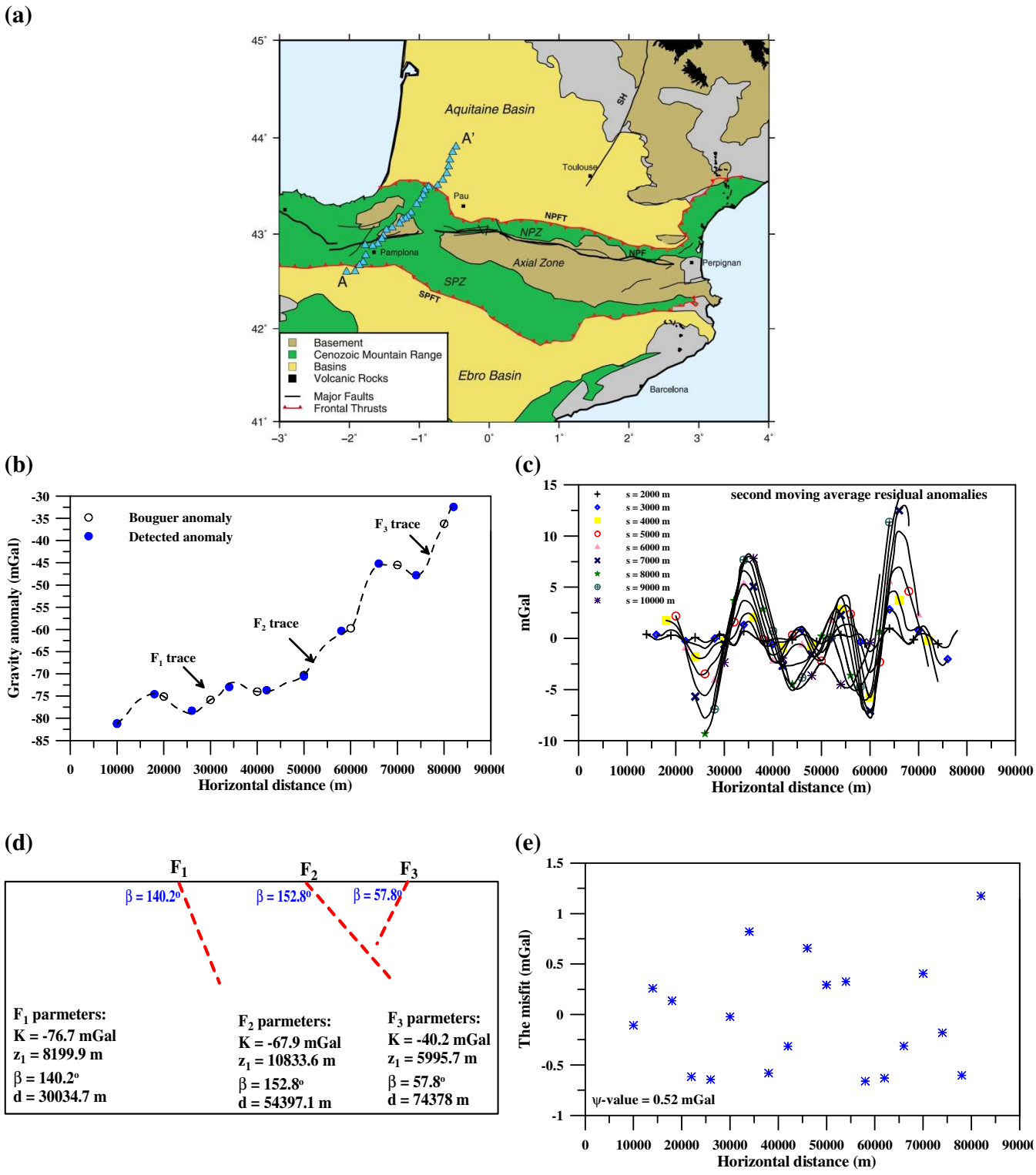
(a)
Aquitaine Basin
A'
A
Toulouse
Pau
Pamplona
Perpignan
Barcelona
Axial Zone
Ebro Basin
SH
NPFT
NPZ
NPF
SPZ
SPFT
Basement
Cenozoic Mountain Range
Basins
Volcanic Rocks
Major Faults
Frontal Thrusts
(b)
Bouguer anomaly
Detected anomaly
F1 trace
F2 trace
F3 trace
Gravity anomaly (mGal)
Horizontal distance (m)
(c)
second moving average residual anomalies
s = 2000 m
s = 3000 m
s = 4000 m
s = 5000 m
s = 6000 m
s = 7000 m
s = 8000 m
s = 9000 m
s = 10000 m
mGal
Horizontal distance (m)
(d)
F1
F2
F3
β = 140.2°
β = 152.8°
β = 57.8°
F1 parmeters:
K = -76.7 mGal
z1 = 8199.9 m
β = 140.2°
d = 30034.7 m
F2 parmeters:
K = -67.9 mGal
z1 = 10833.6 m
β = 152.8°
d = 54397.1 m
F3 parmeters:
K = -40.2 mGal
z1 = 5995.7 m
β = 57.8°
d = 74378 m
(e)
The misfit (mGal)
ψ-value = 0.52 mGal
Horizontal distance (m)

Fig. 8.

Table 1. Numerical results for applying the global particle swarm algorithm to interpret the second moving average residual gravity data using several s-values for a two-sided dipping fault model (K = 100 mGal, z_1 = 4 km, z_2 = 9 km, β = 50°, d = 10 km, and profile length = 100 km) generated and containing a third-order regional background without and with various level of noise.

parameters	Used ranges	Using the global particle swarm algorithm for interpreting gravity data											
		with a 0% noise											
		s = 2 km	s = 3 km	s = 4 km	s = 5 km	s = 6 km	s = 7 km	s = 8 km	s = 9 km	s = 10 km	μ-value	ϕ-value (%)	Ψ-value (mGal)
K (mGal)	50-300	100	100	100	100	100	100	100	100	100	100.0±0	0	
z_1 (km)	1-20	4	4	4	4	4	4	4	4	4	4.0±0	0	
z_2 (km)	1-20	9	9	9	9	9	9	9	9	9	9.0±0	0	0
β (°)	10-180	50	50	50	50	50	50	50	50	50	50.0±0	0	
d (km)	1-20	10	10	10	10	10	10	10	10	10	10.0±0	0	
with a 5% noise													
K (mGal)	50-300	95.2	96.1	96.5	96.8	97.6	97.6	98.3	98.1	98.2	97.2±1.1	2.8	
z_1 (km)	1-20	3.5	3.6	3.6	3.7	3.6	3.7	3.8	3.8	3.8	3.7±0.1	7.5	
z_2 (km)	1-20	8.4	8.5	8.5	8.6	8.7	8.6	8.6	8.8	8.8	8.6±0.1	4.4	9.7
β (°)	10-180	45.6	46.8	46.7	47.3	47.9	48.2	48.6	49.1	49.3	47.7±1.2	4.6	
d (km)	1-20	9.6	9.6	9.7	9.6	9.8	9.7	9.7	9.8	9.8	9.7±0.1	3.0	
with a 10% noise													
K (mGal)	50-300	91.3	92.4	92.3	94.6	95.4	94.6	94.9	96.1	97.2	94.3±1.9	5.7	
z_1 (km)	1-20	3.3	3.4	3.4	3.3	3.5	3.4	3.6	3.7	3.7	3.5±0.2	12.5	
z_2 (km)	1-20	7.8	8.1	8.4	8.5	8.1	8.6	8.4	8.6	8.5	8.3±0.3	7.8	11.6
β (°)	10-180	41.6	43.5	42.8	44.4	46.2	47.8	46.3	45.8	46.5	44.9±2.0	10.2	
d (km)	1-20	9.1	9.3	9.5	9.4	9.7	9.3	9.2	9.5	9.6	9.4±0.2	6.0	

Table 2. Numerical results for applying the present approach to interpret the gravity anomaly for the Kifl oil field faults, Iraq.

models	parameters	Used ranges	Using the global particle swarm algorithm for interpreting gravity data										
			s = 500 m	s = 750 m	s = 1000 m	s = 1250 m	s = 1500 m	s = 1750 m	s = 2000 m	s = 2250 m	s = 2500 m	μ-value	Ψ-value (mGal)
Fault 1 (F1)	K_{11} (mGal)	-10-10	-2.36	-2.35	-2.41	-2.44	-2.47	-2.51	-2.48	-2.45	-2.46	-2.43±0.05	0.07
	z_{11} (m)	500-4000	1686.5	1712.3	1729.5	1748.8	1759.1	1774.9	1762.7	1765.8	1769.4	1745.4± 29.9	
	z_2 (m)	500-4000	2291.5	2312.9	2325.4	2336.7	2346.8	2367.1	2374.6	2364.2	2362.3	2342.4±28.1	
	β_{11} (°)	5-180	48.7	49.2	50.3	51.5	51.4	52.5	52.1	50.1	49.7	50.6±1.3	
	d_{11} (m)	4000-20000	8868.9	8891.1	8910.3	8922.4	8929.3	8939.9	8958.1	8955.4	8961.4	8926.3±31.8	
Fault 2 (F2)	K_{12} (mGal)	-10-10	-2.44	-2.53	-2.58	-2.64	-2.66	-2.71	-2.68	-2.65	-2.63	-2.61±0.08	
	z_{12} (m)	500-4000	1618.4	1620.5	1634.1	1644.8	1649.7	1659.1	1647.7	1645.2	1654.9	1641.6±14.4	
	z_2 (m)	500-4000	2279.9	2306.1	2333.4	2349.7	2371.5	2364.7	2359.8	2355.6	2361.4	2342.4±30.7	
	β_{12} (°)	5-180	37.5	39.1	42.4	44.4	46.2	48.7	45.4	43.5	42.9	43.3±3.5	
	d_{12} (m)	4000-20000	14509.9	14558.1	14600.9	14654.2	14668.9	14689.7	14702.3	14698.5	14683.2	14640.6±68.8	

Table 3. Numerical results for applying the present approach to interpret the gravity anomaly for the Graber oil field faults, USA.

parameters	Used ranges	Using the global particle swarm algorithm for interpreting gravity data										
		s = 500 m	s = 750 m	s = 1000 m	s = 1250 m	s = 1500 m	s = 1750 m	s = 2000 m	s = 2250 m	s = 2500 m	μ-value	Ψ-value (mGal)
K (mGal)	1-10	1.49	1.52	1.53	1.54	1.56	1.62	1.65	1.63	1.64	1.58±0.06	0.02
z_1 (m)	200-2000	686.4	695.8	710.6	716.9	724.7	729.6	735.9	741.2	739.8	720.1± 19.4	
z_2 (m)	-----	-----	-----	-----	-----	-----	-----	-----	-----	-----	-----	
β (^{o})	5-180	120.3	121.8	122	122.7	122.5	123.4	123.9	124.6	123.7	122.8±1.3	
d (m)	2000-20000	7860.7	7901.5	7950.6	7986.9	8000.4	8052.3	8055.1	8035.7	8023.4	7985.2±68.3	

Table 4. Comparative results due to the interpretation of the gravity anomaly for the Graber oil field faults, USA.

parameters	Geologic information (Feris, 1987)	Murthy and Krishnamacharyulu method (1990)	Rao et al. method (2003)	Ekinci et al. method (2019)	The present method
K (mGal)	-----	-----	-----	2.4±0.3	1.58±0.06
z_1 (m)	940	990	620	690±250	720.1±19.4
β (^{o})	-----	135	-----	81.55±7.05	122.8±1.3
d (m)	-----	-----	-----	7890±70	7985.2±68.3

Table 5. Numerical results for applying the present approach to interpret the gravity anomaly for the Gazelle fault example, Egypt.

parameters	Used ranges	Using the global particle swarm algorithm for interpreting gravity data										
		s = 125 m	s = 187.5 m	s = 250 m	s = 312.5 m	s = 375 m	s = 437.5 m	s = 500 m	s = 562.5 m	s = 625 m	μ-value	Ψ-value (mGal)
K (mGal)	0.5-50	3.1	3	3.2	3.3	3.2	3.4	3.4	3.5	3.4	3.3±0.2	
z_1 (m)	50-1500	180.5	185.9	196.3	200.2	205.4	210.7	203.9	205.1	203.8	199.1±9.9	
z_2 (m)	50-1500	385.8	397.1	400.8	412.7	433.5	500.6	521.7	535.4	522.8	456.7±62.1	1.1
β (°)	5-180	52.3	54.9	55.6	57.1	56.8	57.2	55.4	54.9	54.1	55.4±1.6	
d (m)	500-5000	2414.3	2418.9	2426.8	2432.1	2438.1	2438.5	2432.5	2429.8	2430.7	2429.1±8.1	

Table 6. Comparative results due to the interpretation of the gravity anomaly for the Gazelle fault example, Egypt.

parameters	Drilling information (Evans et al., 1991)	Abdelrahman et al. method (2013)	Essa method (2013)	Abdelrahman and Essa method (2015)	The present method
K (mGal)	-----	-----	-----	2.4±0.3	3.3±0.2
z_1 (m)	200	173	208	202±0.017	199.1±9.9
z_2 (m)	-----	-----	-----	-----	456.9±62.1
β (°)	-----	62.5	40	57.7±4	54.4±1.6
d (m)	-----	-----	-----	-----	2429.1±8.1

Table 7. Numerical results for applying the present approach to interpret the gravity anomaly for the Mersa Matruh fault example, Egypt.

parameters	Used ranges	Using the global particle swarm algorithm for interpreting gravity data										
		s = 900 m	s = 1350 m	s = 1800 m	s = 2250 m	s = 2700 m	s = 3150 m	s = 3600 m	s = 4050 m	s = 4500 m	μ-value	Ψ-value (mGal)
K (mGal)	0.5-50	13.4	13.7	14.3	14.5	14.6	14.7	15.1	15.3	15.4	14.6±0.7	
z_1 (m)	500-5000	3820.1	3882.4	3924.7	3968.6	3998.1	4052.3	4102.9	4186.3	4195.4	4014.5±130.9	
z_2 (m)	500-6000	4415.6	4459.8	4661.4	4705.7	4735.1	4774.6	4786.9	5025.3	5098.9	4740.4±224.9	0.2
β (°)	5-180	85.4	86.7	88.1	86.8	87.9	88.1	88.2	90.1	91.5	88.1±1.8	
d (m)	5000-40000	21680.5	21689.8	21701.5	21725.6	21755.8	21782.7	21801.9	21824.6	21834.3	21755.2±58.8	

Table 8. Comparative results due to the interpretation of the gravity anomaly for the Mersa Matruh fault example, Egypt.

parameters	Drilling information (Barakat and Darwish (1984))	Abdelrahman and Essa method (2013)	Anderson et al. method (2020)	The present method
K (mGal)	-----	-----	13.71	14.6±0.7
z_1 (m)	>4000	3940 ± 661	3982.5	4014.5±130.9
z_2 (m)	-----	-----	-----	4740.4±224.9
β (°)	-----	-----	-----	88.1±1.8
d (m)	-----	-----	-----	21755.2±58.8

Table 9. Numerical results for applying the present approach to interpret the gravity anomaly for the Pyrenees fault, France.

models	parameters	Used ranges	Using the global particle swarm algorithm for interpreting gravity data										
			s = 2000 m	s = 3000 m	s = 4000 m	s = 5000 m	s = 6000 m	s = 7000 m	s = 8000 m	s = 9000 m	s = 10000 m	μ-value	Ψ-value (mGal)
F_1	K (mGal)	-10--100	-74.6	-75.2	-75.8	-76.7	-77.5	-77.9	-77.4	-77.5	-77.3	-76.7±1.2	0.52
	z_1 (m)	2×10^3-2×10^4	7821.1	8060.2	8104.9	8199.7	8285.4	8326.8	8263.3	8349.4	8388.9	8199.9±179.4	
	z_2 (m)	-----	-----	-----	-----	-----	-----	-----	-----	-----	-----	-----	
	β (°)	5-185	135.6	137.8	140.4	140.8	140.9.3	142.1	141.4	141.8	141.5	140.2±2.3	
	d (m)	10^4-9×10^4	29456.5	29667.8	29761.3	29931	30056.7	30122.4	30154.2	31012.8	30150.2	30034.7±439.7	
F_2	K (mGal)	-10--100	-66	-66.8	-67.5	-67.7	-67.9	-68.1	-68.4	-68.9	-69.4	-67.9±1.0	
	z_1 (m)	2000-20000	10453.7	10711.9	10789.5	10842.2	10886.7	10904.1	10956.8	10982.1	10975.4	10833.6±168.2	
	z_2 (m)	-----	-----	-----	-----	-----	-----	-----	-----	-----	-----	-----	
	β (°)	5-185	149.7	151.4	152.3	152.9	153.7	154.2	153.4	153.6	153.8	152.8±1.4	
	d (m)	10^4-9×10^4	53541.2	53912.9	54214.7	54322.2	54510.8	54623.2	55074.6	54761.8	54612.7	54397.1±462.1	
F_3	K (mGal)	-10--100	-38.7	-39.5	-39.8	-40.1	-40.4	-40.9	-41.2	-40.8	-40.5	-40.2±0.8	
	z_1 (m)	2000-20000	5601.4	5832.4	5943.8	6023.7	6069.8	6098.1	6101.1	6124.7	6165.9	5995.7±179.7	
	z_2 (m)	-----	-----	-----	-----	-----	-----	-----	-----	-----	-----	-----	
	β (°)	5-185	55.9	56.4	56.7	57.2	57.9	58.6	59.3	58.7	58.8	57.8±1.2	
	d (m)	10^4-9×10^4	73489.7	73786.1	74056.1	74264.9	74547.3	74610.5	74789.7	75044.6	74813.2	74378±517.4	